

submitted to *Geophys. J. Int.*

Forward and Inverse Mantle Convection with Neural Operators

Chenxi Kong¹, Michael Gurnis¹ and Zachary E. Ross¹

¹ *Seismological Laboratory, California Institute of Technology, Pasadena, CA 91125, USA.*

SUMMARY

Thermal state reconstruction—reversing convection to recover the thermal structure of the mantle at an earlier geologic time—is an important tool to understand the evolution of mantle convection and its relation to seismic tomographic images and observations at the surface. Thermal state reconstructions are computationally expensive. Here we transformed the basic computational element, numerical solvers, into neural operators, a class of machine learning models for learning mappings between function spaces. Focusing on a specific architecture, Fourier Neural Operators, we demonstrate that they can represent not only a surrogate model like the Stokes system of equations using a purely physics informed approach, but also discover operators without explicit mathematical formulations or even ill-posedness from data, including the direct mapping between two convecting thermal states separated by a long time interval much larger than the Courant Fredrich Lewy condition and its reversal. These neural operators significantly accelerate forward and inverse convection modeling by transforming forward physical processes into surrogate models with lower complexity while utilizing auto-differentiation to calculate gradients. With this framework, we demonstrate the strength and weaknesses of four methods for thermal state reconstructions: Reverse buoyancy, reverse convection operator, an inversion with only the terminal thermal state, and a joint inversion with the

terminal thermal state and surface velocity evolution. The reverse convection operator is shown to perform poorly in the presence of observational noise, but the joint inversion overcomes this limitation. The joint technique could probably become a solution to large-scale thermal state inversion problems using seismic tomography and plate tectonic reconstructions.

Key words: Mantle convection, Inverse Theory, Machine Learning, Neural Operators, Dynamic System.

1 INTRODUCTION

Plate kinematics, the subsidence and cooling of oceanic plates, and the life cycle of plates demonstrates that plates make up the upper thermal boundary layer of mantle convection (Davies 1999). Central to this concept is that plate motions reflect the surface, horizontal velocity field of convection. With advances in seismic tomography, a more detailed picture of the present day mantle, and hence the temperature field of mantle convection, has gradually emerged (e.g., Ritsema et al. 2011; Koelemeijer et al. 2016; Lu et al. 2019). If we can construct a self-consistent dynamic framework of the present Earth (the dynamics that links the driving temperature field with the surface kinematics), the possibility opens that we can build ones for earlier times, especially in light of the extensive constraints that exist for past plate motions (e.g., Seton et al. 2012; Merdith et al. 2021).

Such a framework could be based on a forward model describing the mantle dynamics. Forward models have successfully reproduced many features of plate tectonics, such as ones that model global plate motions (e.g., Hager & O'Connell 1981; Conrad & Lithgow-Bertelloni 2002; Stadler et al. 2010; Hu et al. 2024), those that attempt to simulate plate tectonics (e.g., Van Heck & Tackley 2008; Becker & Fuchs 2023), or those that produce realistic subduction (e.g., Zhong & Gurnis 1995; Billen 2008; Goes et al. 2017). Such later plate tectonic and subduction models are initiated from a specified state in parameter space and produce evolutionary pathways. The models which best fit a set of observations, such as plate kinematics and present-day mantle structure, then partially reveal the physics underlying the tectonic process. However, there exist substantial uncertainties within a large parameter space and finding the optimal model is often difficult.

Beside forward modeling trials, other approaches have been explored, including those aimed at reconstructing a previous mantle state, or reversing mantle convection (e.g., Conrad

& Gurnis 2003; Bunge et al. 2003; Ismail-Zadeh et al. 2004; Liu & Gurnis 2008; Li et al. 2017). As mantle convection is dissipative and irreversible, reconstructing prior states is an ill-posed problem and cannot be solved directly. Consequently, the reconstruction problem is usually solved through an inverse approach, overcoming the ill-posedness, while allowing additional information to be used as constraints (Kirsch et al. 2011). As alluded to, there exist rich chronological data preserved at Earth’s surface providing records of surface imprints of interior dynamics. Those data are taken in various forms including but not limited to: Plate kinematics inferred from seafloor spreading, paleomagnetic reconstruction of continental motions, and hot spot tracks (e.g., Engebretson et al. 1985; Steinberger & O’Connell 1998; Torsvik et al. 2007; Seton et al. 2012); topography revealed by stratigraphic sequences and past sea level changes (e.g., Gurnis 1993; Spasojevic et al. 2009); mantle flow history recorded within mineral anisotropy (e.g., Ribe 1989; Long & Becker 2010); and subduction and intraplate deformations preserved in exhumed and magmatic rock sequences (e.g., Ernst 1988; Harris et al. 1986). Besides the chronological data, the terminal state—the observed present-day mantle—provides direct constraint across the entire mantle depth. The observables are connected to the system state variable, the thermal structure of the mantle, through a fully dynamic and self-consistent forward model. With an objective function, mismatch between model predictions and observables, the update direction of the initial state can be calculated by solving the adjoint state equations and optimized towards that initial state by iterative gradient descent.

Although a gradient descent method has guided optimization directions that avoids empirical trials, it still relies on an iterative approach. Consequently, inversions have a high computational cost which can be several orders of magnitude larger than one forward model (Li et al. 2017). Solving the forward and adjoint convection equations iteratively with traditional PDE solvers is computationally demanding and has limited its applicability for geophysical inversions. Leaving aside the iterations, solving the forward model itself (and its adjoint) can be expensive as well. To model realistic mantle dynamics with plate tectonics requires both a long temporal scale and a fine spatial resolution at plate boundaries, as plates recycle (Billen 2008; Hu et al. 2024) over hundreds of million years (Zhang et al. 2010). A global reconstruction that incorporates realistic, evolving plate tectonics, is computationally intractable with traditional numerical methods.

We attempt to overcome this challenge, by reformulating the governing equations of thermal convection into a surrogate model with a neural operator (Kovachki et al. 2023). With the rapid development in machine learning, there have been studies using deep learning approaches

in mantle dynamics modeling and inversions. Atkins et al. (2016) and Shahnas et al. (2018) used neural networks to infer the controlling parameters in convection from synthesized thermal fields, but not within an inverse approach. Later, Agarwal et al. (2021, 2025) formulated a convolutional neural network (CNN, LeCun et al. (2002)) from computations of thermal convection. The surrogate models shows an appealing speed up in forward modeling, but their accuracy in tracking long-term unsteady convection is insufficient to capture the motion of plume structures, and they have not yet been applied to inverse problems. Neural operators inherits almost all of the advantages of a common neural network, including fast computations (evaluation) once trained for both forward and backward solves. Architecturally, it is designed to learn the integral kernel of mappings instead of point-wise connections between nodal values; the inputs and outputs are not forced to be discretized on a specific mesh and the neural operators learn the mappings between function spaces. The most common scenario is to learn a given partial differential equation (PDE) operator. Neural operators can also learn mappings that cannot normally be explicitly described mathematically or numerically solved, collectively known as operator discovery. Consequently, neural operators have been widely used in scientific computations (Azizzadenesheli et al. 2024), including for fluid dynamics applications to turbulent flow (Navier-Stokes), Darcy flow, Stokes flow, and Rayleigh–Bernard convection (Li et al. 2020; Marwah et al. 2023; Straat et al. 2025). In geophysics, examples include learning the operator for seismic wave propagation and its incorporation into full waveform inversion (Yang et al. 2021; Zou et al. 2024, 2025). Various neural operator architectures are emerging, among which the Fourier neural operator (FNO), which parameterizes the kernel in Fourier space, has been extensively used and has been shown to be robust for high accuracy operator learning (Li et al. 2020). Here, we use FNO as the basic neural operator architecture. We test various possibilities for the usage of neural operators in modeling forward and reverse mantle convection. We find that this surrogate approach can significantly accelerate both forward and inverse computation, while keeping a total workflow cost (including training) comparable to that of performing a time-dependent inversion only once by a traditional numerical method.

2 METHODOLOGY

2.1 Thermal Convection Problem

The mantle is treated as an incompressible, creeping viscous fluid. Assuming chemical homogeneity, its convection is simplified to a basally-heated thermal convection within a 2-D Cartesian domain Ω , which is governed by the conservation of mass, momentum, and energy

(Zhong et al. 2000):

$$\nabla \cdot \mathbf{u} = 0 \quad (1)$$

$$\nabla p + \nabla \cdot (\eta \nabla \mathbf{u}) - \alpha \rho_0 (T - T_0) e_z = 0 \quad (2)$$

$$\frac{\partial T}{\partial t} + \mathbf{u} \cdot \nabla T - \nabla (\kappa_T \nabla T) = 0 \quad (3)$$

where \mathbf{u} , p , η , α , ρ_0 , T , T_0 , and κ_T are velocity, dynamic pressure, dynamic viscosity, thermal expansitivity, reference density, temperature, reference temperature, and thermal diffusivity respectively. η , α , and κ are set as constant values. By normalizing with $\eta = \eta_0$, $\alpha = \alpha_0$, $\kappa = \kappa_0$, $x = Dx'$, $p = \frac{\eta_0 \kappa_0}{D^2} p'$, $\mathbf{u} = \frac{\kappa_0}{D} \mathbf{u}'$, and $T = \Delta T T' + T_0$, and dropping the primes subsequently, we have the dimensionless governing equations,

$$\nabla \cdot \mathbf{u} = 0 \quad (4)$$

$$\nabla p + \nabla \cdot \nabla \mathbf{u} - \text{Ra} T e_z = 0 \quad (5)$$

$$\frac{\partial T}{\partial t} + \mathbf{u} \cdot \nabla T - \nabla^2 T = 0 \quad (6)$$

where $\text{Ra} = \frac{\rho g \alpha_0 \Delta T D^3}{\eta_0 \kappa_0}$ is the Rayleigh number. For the unknowns, we introduce their solution spaces defined on Ω , that $\mathbf{u} \in \mathcal{U}$, $p \in \mathcal{P}$, $T \in \mathcal{T}$. The governing equations can be decomposed into two sets: the Stokes (Eq. 4, 5) and the advection-diffusion (Eq. 6). The Stokes equations solve velocities from the buoyancy field determined by temperature: $\mathbf{S} : \mathcal{T} \rightarrow \mathcal{U}$. The advection-diffusion equation integrates advection $\mathbf{A} : (\mathcal{T}, \mathcal{U}) \rightarrow \mathcal{T}$ and diffusion $\mathbf{D} : \mathcal{T} \rightarrow \mathcal{T}$ on T for a time step, Δt , where \mathbf{S} , \mathbf{A} , \mathbf{D} denote their solution operators. The solutions to both equations are subject to the boundary conditions. For the Stokes, we assume no-slip conditions on the top and bottom and for the advection-diffusion equation, we assume a Dirichlet boundary condition for temperature, where $T = 0$ at the top and $T = 1$ at the bottom. For the side walls, periodic boundary conditions are assumed.

Traditionally, the solution of the two components is interwoven and the dynamic process of thermal convection emerges. Numerical methods, such as the finite element method (FEM) (e.g., Christensen 1984) or finite differences (FD) (e.g., Gerya 2019), have applied for the solves. Powerful software tools have emerged for the study of geodynamic problems in recent decades and we use an open source, well-benchmarked FEM-based program, **Underworld**, as the numerical solver for creating sample and validation data (Mansour et al. 2020). An example computation from **Underworld** is given in Fig. 1, where the Rayleigh number is 10^7 with the domain discretized with 256×256 linear elements; the numerical procedure used will be detailed below. The computation is initiated with a random Gaussian thermal field that satisfies the boundary conditions, and is integrated forward for about 34 transit times, t_{tr} , a

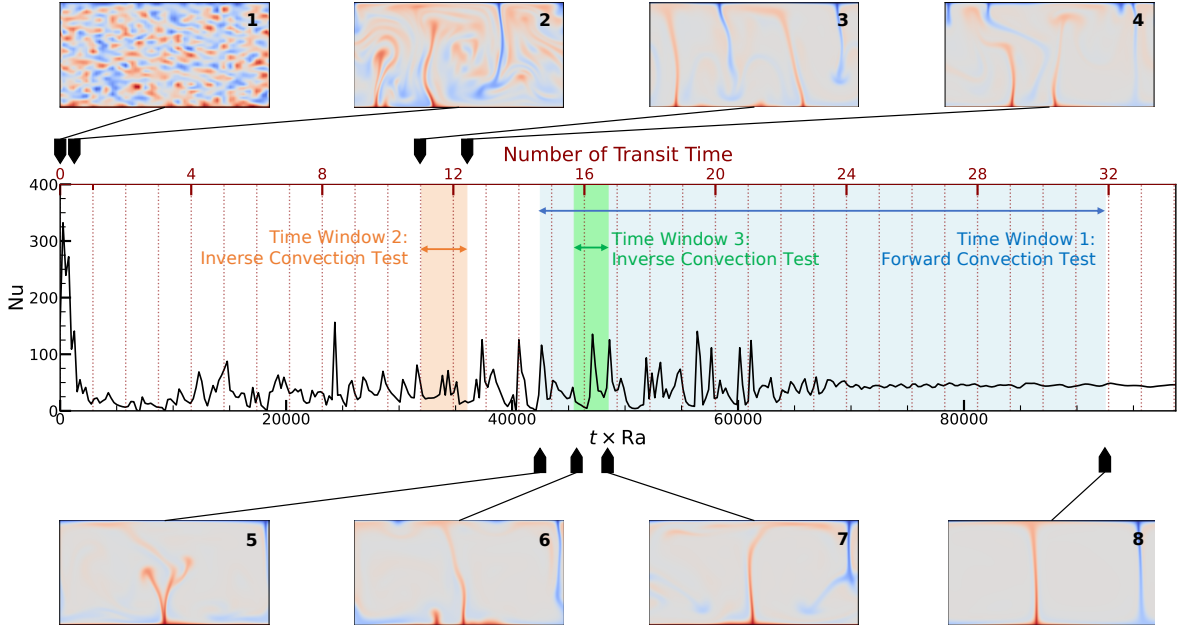


Figure 1. An example of forward convection computed with `Underworld`, which is used as an evaluation data sequence in this study. The computation is initiated from a Gaussian random initial thermal field that satisfies the prescribed boundary conditions. The total integration time is around 34 transit times, during which the convection pattern evolves from a chaotic one to a relatively steady state, as shown by the tracked Nusselt number. The temperature field is displayed at eight instances to depict the thermal evolution.

characteristic time defined as that needed for a point to traverse the box depth. For the Earth, the transit time is ~ 50 Myrs (Zhong et al. 2007). With traditional solvers, the time step size of each forward integration is limited by the Courant Fredrich Lewy (CFL) condition (Courant et al. 1928). In the following discussion, we will show that neural operators can circumvent this limit, greatly accelerating computations. Assuming a constant, maximum Δt that could satisfy the limit throughout the evolving sequence, the computation can be described as applying an autoregressive operator $\mathbf{F}^{\Delta t} : \mathcal{T} \rightarrow \mathcal{T}$ recursively on a state variable of T , by which we define $\mathbf{F}^{\Delta t}$ as:

$$\begin{aligned} \mathbf{F}^{\Delta t}(\cdot) &:= \mathbf{I}(\cdot) + \Delta t(\mathbf{A}(\cdot, \mathbf{u}) + \mathbf{D}(\cdot)) \\ &= \mathbf{I}(\cdot) + \Delta t(\mathbf{A}(\cdot, \mathbf{S}(\cdot)) + \mathbf{D}(\cdot)) \end{aligned} \quad (7)$$

with $\mathbf{F}^{n\Delta t} := (\mathbf{F}^{\Delta t})^n$ is the mapping from an initial thermal state to a future one at $n\Delta t$.

2.2 Thermal State Reconstruction

In addition to the forward solution of mantle convection, we are concerned with its evolution through reconstructing previous states from observations. One must first address whether a

previous thermal state can be reconstructed as thermal convection is dissipative: New information is generated with amplitudes magnified at thermal boundary layers, but then vanishes into noise through advection and diffusion. With the diffusion time scaling in proportion to the square of size, the finest structures diffuse most rapidly, while the larger has a longer, persistent influence, perhaps extending over a substantial period of geologic time. Within a finite duration, some dominant, longer wavelength features will likely still be recoverable from the remnants, although lacking reliable high-frequency details. This is the basis that supports the feasibility of mantle state reconstruction.

A potential avenue for reconstructing a previous thermal state is to temporally reverse convection by replacing the forward time t in Eq. 4 to 6 with $-s$, which is the reversal time.

$$\nabla \cdot \mathbf{u} = 0 \quad (8)$$

$$\nabla p + \nabla \cdot \nabla \mathbf{u} - \text{Ra} T e_{\mathbf{z}} = 0 \quad (9)$$

$$\frac{\partial T}{\partial s} - \mathbf{u} \cdot \nabla T + \nabla^2 T = 0 \quad (10)$$

Similar to the forward problem, Eq. 8 to 10 forms an operator $\mathbf{F}^{-n\Delta t}$, that maps a thermal field to its past state at $-n\Delta t$. However, $\mathbf{F}^{-n\Delta t}$ is ill-posed. The forward dynamics forms a dissipative system that tends to compress the state trajectory into an attractor (Fig. 1). In contrast, the reverse dynamics system is expansive in which any noise is magnified rapidly because of the existence of the anti-diffusion operator, the negative Laplacian. If one attempts to solve Eq. 8 to 10 with numerical methods directly, the amplified error in the thermal field grows rapidly within several CFL time steps. Hence, a simple but inaccurate approach to reversing convection is to retain the diffusion process while integrating backwards (Conrad & Gurnis 2003), where the advection diffusion equation reads:

$$\frac{\partial T}{\partial s} - \mathbf{u} \cdot \nabla T - \nabla^2 T = 0 \quad (11)$$

which only reverses the direction of advection, or the sign of the buoyancy force. We will call this the 'reverse buoyancy method'.

As to be detailed subsequently, important improvements for thermal state reconstructions can be made with neural operators. We will approximate the ill-posed operator $\mathbf{F}^{-n\Delta t}$ directly with a neural substitute $\mathbf{F}_{\phi}^{-n\Delta t}$ capable of suppressing the rapid magnification of numerical noise. That is, we will train a neural operator that aims to make the most informative prediction directly towards a previous state by the limit of diffusion.

Nevertheless, the approximated reverse convection neural operator is still sensitive to the noise within the input, making its application in geophysical problems limited and dif-

ficult. Hence, the reconstruction problem has been commonly regarded as an inverse problem covering a temporal scope $[-N \times n\Delta t, 0]$ with the target being a past mantle state $T_0 := T(t = -N \times n\Delta t)$ (Bunge et al. 2003; Ismail-Zadeh et al. 2004; Liu & Gurnis 2008; Li et al. 2017). Inverse methods are more robust against observational noise. Similar to the direct methods mentioned above where only the observation of the terminal thermal state is utilized, the inversion can be formulated simply by a fit to the terminal state. However, the constraint can also take in various forms of observational data beyond that; this is important with the rich chronological records constraining mantle evolution. We will later demonstrate that compared with the inversion using the terminal thermal state only, incorporation of chronological data could greatly improve the accuracy of inversion and enlarge the time span for reconstruction. By contrast, this approach is named 'joint inversion', where two classes of observations are used. First, information on present-day mantle structure defined in Ω , often revealed by seismic tomography (or other geophysical imaging); Second, chronological data defined along the time axis on the top boundary L_s , such as surface horizontal velocity records (corresponding to plate kinematics) $\mathbf{v}_x^{\text{obs}}(t), t \in [-N \times n\Delta t, 0]$. For simplicity, we assume that the terminal thermal state $T_N := T(t = 0)$, and $\mathbf{v}_x^{\text{obs}}(t)$ are known. The two constraints are applied through the governing equations by connecting the inversion target to the observations.

The inversion is conducted through an iterative approach. We will use superscript k to denote the iteration step index. When $k = 0$, one would need to start from an initial guess to the target state T_0^0 , and compute the forward evolution process to determine the values of diagnostic variables, which correspond to observations, i.e., the surface velocity of each time step $\mathbf{v}_{x,i}^0, i = 0, \dots, N$, and the mantle thermal field at $t = N \times n\Delta t$, defined as T_n^0 . Then, by comparing the computed diagnostic variables to observations, we calculate the objective function (Modified from Li et al. 2017)

$$\mathcal{J}^k = \frac{\beta_1}{|\Omega|} \int_{\Omega} (T_N^k - T_N^{\text{obs}})^2 dw + \frac{\beta_2}{n|L_s|} \sum_{i=0}^n \int_{L_s} (\mathbf{v}_i^k - \mathbf{v}_i^{\text{obs}})^2 dl + \mathcal{P}(T_0^k) \quad (12)$$

where $|\cdot|$ denotes the Lebesgue measure of a subdomain in which the diagnostic variables are evaluated. The first and second terms evaluate the misfits between the model predictions and observations of terminal state and surface horizontal velocities. The regularization function \mathcal{P} combines Laplacian smoothing and a penalty on departures of the initial state from its spatial mean T_{mean} :

$$\mathcal{P}(T_0^k) = \frac{1}{|\Omega|} \int_{\Omega} \left(\beta_3 (\nabla^2 T_0^k)^2 + \beta_4 (T_0^k - T_{\text{mean}})^2 \right) dw \quad (13)$$

β_1 to β_4 are weighting coefficients of each term (Table S4). Then, a gradient of the objective

function with respect to the target state, $\nabla_{T_0^k} \mathcal{J}^k$, from which the target state can be updated through gradient descent by the Adam algorithm (Kingma & Ba 2014):

$$T_0^{k+1} = T_0^k - \alpha_k \cdot \text{Adam} \left(\nabla_{T_0^k} \mathcal{J}^k \right) \quad (14)$$

In traditional numerical methods, $\nabla_{T_0^k} \mathcal{J}^k$ is calculated by solving the adjoint equation, which shares a similar form as the forward computation. The total computational cost would be proportional to the product of time steps and the iteration steps, making the inversion typically several orders of magnitude more demanding than the forward problem (e.g., Li et al. 2017). In cases where the solution to $\mathbf{F}^{n\Delta t}$ is already expensive, the mantle state reconstruction would then be computationally prohibitive. Hence, this motivates the use of neural operators to replace the numerical solvers in thermal reconstruction problems.

In all, four different reconstruction methods are formulated in this study, and their performances are compared against each other: (1) reverse buoyancy; (2) reverse convection neural operator; (3) inversion with forward convection neural operator using the terminal state only; and (4) joint inversion with forward convection neural operator.

2.3 Neural Operators

Given geodynamic forward models and mantle state reconstructions (consisting of repeated computation of $\mathbf{F}^{\Delta t}$), the workflow would be significantly accelerated if this basic operation could be replaced with a faster and less costly approach. This is the inspiration for a new deep learning workflow as a replacement for the PDE-formulated operator, utilizing rapidly developing technology in machine learning and GPU computing. The approach transforms the problem of solving PDEs into a forward pass through a deep learning model, while computing derivatives on a clearly structured, net-shaped computational graph with fast auto-differentiation (Griewank & Walther 2008). Neural operators are a class of models that generalize neural networks to function spaces and are universal approximators of non-linear operators Kovachki et al. (2023). In general, it approximates a functional mapping $\mathcal{G} : \mathcal{A} \rightarrow \mathcal{U}$ with the following architecture \mathcal{G}_ϕ , parameterized by the trainable ϕ :

$$\begin{aligned} h_0(x) &= P(a(x)) \\ h_{i+1}(x) &= \sigma \left(Wh_i(x) + \int \kappa_\phi(x, y, h_i(x), h_i(y)) h_i(y) dy + b(x) \right) \quad i = 0, 1, \dots, D-1 \quad (15) \\ u(x) &= Q(h_D(x)) \end{aligned}$$

A neural operator first encodes the input function $a \in \mathcal{A}$, into one with a larger codomain $h_0 = P(a)$. Then, h_0 is passed through D layers which each contains a local operator W , an integral kernel κ_ϕ where the parameter ϕ enters, and a bias function b . Afterwards, h_D is decoded into the output function $u \in \mathcal{U}$ by $u = Q(h_D)$. By learning a mapping between function spaces, rather than vector spaces, Neural Operators are *discretization agnostic*, meaning that a model with fixed ϕ satisfies the following properties: (1) it can be applied to any discretizations of the input function, (2) it can be evaluated at any point of the output domain, and (3) it provably converges to the continuum operator as the number of mesh points is refined (Kovachki et al. 2023). Similarly to neural networks that compose linear transformations with non-linear activation functions, neural operators compose linear integral operators with activation functions to achieve universal approximation of non-linear operators.

FNO is a particular type of Neural Operator that evaluates the kernel integration in the Fourier domain for increased speed (Li et al. 2020), that:

$$\begin{aligned} h_{i+1} &= \sigma\left(Wh_i + \mathcal{F}^{-1}(\mathcal{F}(\kappa_\phi) \cdot \mathcal{F}(h_i)) + b\right) \\ &= \sigma\left(Wh_i + \mathcal{F}^{-1}(R_\phi \cdot \mathcal{F}(h_i)) + b\right) \end{aligned} \tag{16}$$

where W_ϕ is a linear transformation on h_t and \mathcal{F} and \mathcal{F}^{-1} are Fourier and inverse Fourier transforms, respectively. The encoding P , and decoding Q , are performed through point-wise multilayer perceptions (MLPs). Each layer is now defined as a Fourier block (FB). Inside the Fourier block, the representation h_i with large co-domain is convolved with the integral kernel κ_ϕ parameterized in Fourier spaces, R_ϕ . This kernel structure is capable of capturing the global information by the nature of convolution, which is also an essential feature that leads to the success of CNNs (LeCun et al. 2002). But unlike the CNN, as R_ϕ is defined in Fourier space, it is actually a mesh-free integral kernel that is independent of the way the input function is discretized in domain Ω , making its performance substantially better than point-wise mappings (Li et al. 2020). However, FNO uses FFTs to evaluate Fourier transforms, which restricts the functions to be on regular grids with the same discretization for output u and input a ; this is not an issue for the present paper, and it is important to note that other neural operator architectures are not restricted to regular grids (Li et al. 2023; Alkin et al. 2024; Shi et al. 2025). Since the learning is accomplished in a Fourier space, the resolutions of g and f can be arbitrarily changed during training or evaluation, as long as the grid remains regular. For instance, the neural operator can be trained by loss evaluated on a low resolution mesh, but can be further evaluated on data with higher resolution. This approach is known as super-resolution evaluation (Kovachki et al. 2023), that both saves the

training cost and generalizes the application scenarios of a trained neural operator, especially for mappings whose underlying physics is scale invariant (Li et al. 2020). This feature will also be demonstrated here.

The major architectural hyperparameters that control the complexity and size of the FNO include the number of FB (model depth), the width of FB (model width), and the maximum number of Fourier modes, as FNO does not have to process information on all frequencies in the latent space but can instead make a low-pass cutoff at this mode. To reduce the model size and save on training costs, we adopted an FNO variant, the tensorized Fourier neural operator (TFNO), in which the number of trainable parameters can be greatly reduced by a global factorization on the tensorized parameters (Kossaifi et al. 2023).

Our first example application of neural operators is as an approximation of the Stokes operator, \mathbf{S} , which is defined by the Stokes equations (Eq. 4, 5). This is an example of learning an operator explicitly formed by a PDE. In addition, neural operators can also be trained to model hidden relationships between function spaces that lack explicit analytical forms or are intractable to solve numerically. Such procedures are commonly referred to as operator discovery. Some of those mappings could play a role in important connections found in mantle dynamics. A straight-forward example is the forward convection operator $\mathbf{F}_{\Delta t}^n$. As described above, the numerical evaluation of this operator requires recursive solutions of the Stokes equation and advection-diffusion equation, while a PDE system that directly maps the initial thermal state to the final one separated by a long time interval does not exist in closed form. The total number of recursive steps depends on the CFL condition, which can be large when modeling full mantle convection problems. The neural operator $\mathbf{F}_{\phi}^{n\Delta t}$ approximates the mapping between two thermal states across an interval much larger than CFL time steps, which significantly shortens the length of the computational chain and reduces the integration steps required. Such a transformation reduces the time complexity of convection time-integration from $O(N^{3/2})$ with numerical methods to sub- $O(N \log(N))$, effectively dominated by a constant term determined by the size of neural operator, within the considered range of N in this study (see supplementary material). It creates cost savings for both forward modeling and the gradient calculation for inverse problems. Another example of model discovery with neural operators is approximating the ill-posed temporal reverse convection operator $\mathbf{F}_{\phi}^{-n\Delta t}$ that maps from the current thermal state to a previous one.

In this study, we will demonstrate how three categories of neural operators (Fig. 2) can be applied to the computation of mantle dynamics: (1) Solving velocity from thermal fields using the Stokes neural operator \mathbf{S}_{ϕ} ; (2) solving the thermal convection problem using $\mathbf{F}_{\phi}^{+n\Delta t}$;

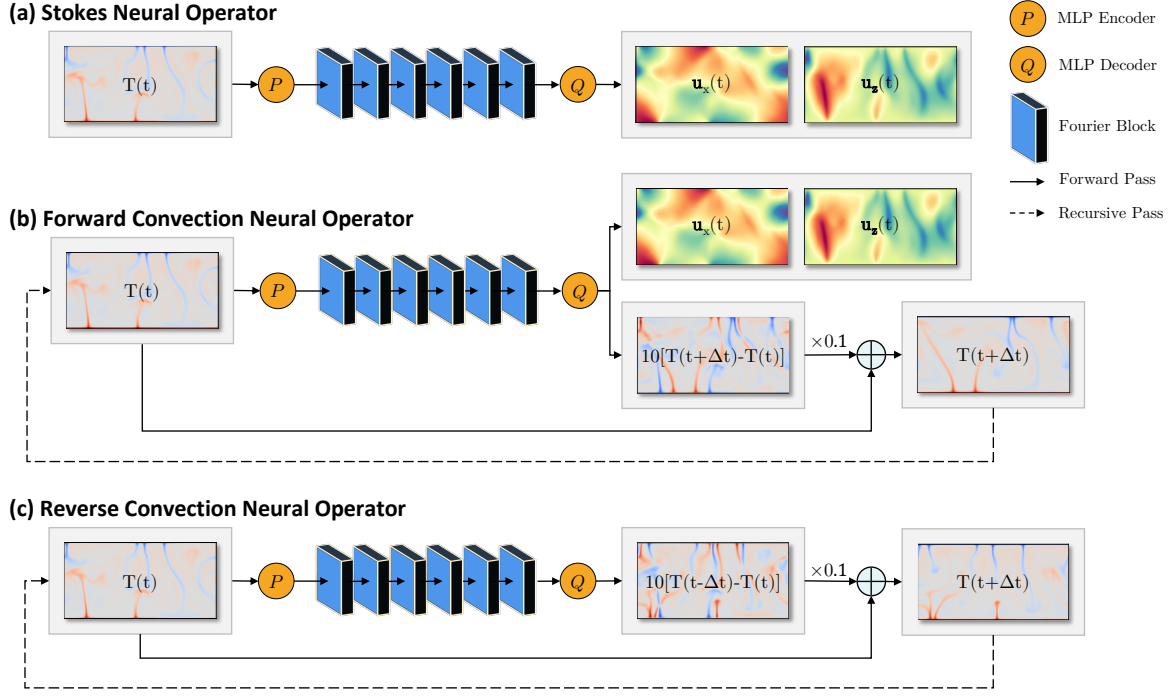


Figure 2. The architecture of three neural operators described in this study. Detailed MLP and FB parameters are listed in Table S1.

and (3) application of neural operators to thermal state reconstruction, including a fast and direct method using $\mathbf{F}_\phi^{-n\Delta t}$, and a robust inverse method using $\mathbf{F}_\phi^{+n\Delta t}$.

2.3.1 Stokes neural operator

The Stokes neural operator, \mathbf{S}_ϕ , solves the Stokes equation for velocity and pressure from buoyancy and is the most computationally demanding part of the traditional solution of mantle convection. It takes a temperature field as the source term (input), and outputs velocity and pressure as a response (Fig. 2a). Assuming a constant viscosity, the Stokes operator is linear and its neural approximation is trained with an arbitrary, fixed Rayleigh number and evaluated on systems with other Rayleigh numbers by rescaling outputs.

Similar to other neural architectures, neural operators can be trained using both data-driven and physics-informed approaches. Data-driven methods have a simple form of loss evaluated directly from the deviation between prediction and ground-truth, which can be acquired from forward numerical models. A drawback of this approach emerges when there is insufficient training data, or the high-resolution training data is costly to acquire; in such cases, using the known physical laws to formulate the training loss can greatly reduce the demand on the data as well as the pre-training cost (Raissi et al. 2019; Li et al. 2021). For

mappings that can be expressed explicitly in terms of PDEs, the physics-informed approach can be conducted by a loss based on the PDE structures. We will demonstrate this by training \mathbf{S}_ϕ with a purely physics-informed approach. The loss function takes in the physical constraints as

$$L_C = \beta_{C1} \|\nabla \cdot \mathbf{u}\|_2^2 + \beta_{C2} \|(T - 0.5) \nabla \cdot \mathbf{u}\|_2^2 \quad (17)$$

$$L_M = \|\beta_p \nabla p + \nabla \cdot \nabla \mathbf{u} - \beta_u \text{Ra} T e_{\mathbf{z}}\|_2^2 \quad (18)$$

$$L_B = \|\mathbf{u}_{\mathbf{z}}(z = 0)\|_2^2 + \|\mathbf{u}_{\mathbf{z}}(z = L_z)\|_2^2 + \|\mathbf{u}(x = 0) - \mathbf{u}(x = L_x)\|_2^2 + \|p(x = 0) - p(x = L_x)\|_2^2 \quad (19)$$

$$L_N = \left(\int_{\Omega} \mathbf{u}_x dw \right)^2 \quad (20)$$

$$L_S = \beta_C L_C + \beta_M L_M + \beta_B L_B + \beta_N L_N \quad (21)$$

where L_C , L_M , L_B , L_N , and L_S are continuity, momentum, boundary, net horizontal velocity (as the model is periodic in the horizontal direction), and total Stokes PDE losses respectively, and $\|\cdot\|_2$ is the L_2 norm. The gradient optimization forces the neural operator to generate \mathbf{u} and p that satisfy conservation and boundary conditions. Those loss terms are evaluated using finite differences, a fast and simple algorithm to execute on GPUs (Gerya 2019) (see supplementary material). The weighting coefficients, β_C , β_M , β_B , and β_N are applied on each loss term to balance the weights between conservation and boundary conditions. β_{C1} and β_{C2} are used to balance between two types of continuity constraints, velocity divergence, and divergence weighted with excess temperatures. The latter one aims at forcing the model to concentrate more on the continuity near thermal anomalies. β_u and β_p , are used to rescale velocity and pressure from the neural operator's normalized outputs to its original magnitudes within the (dimensionless) governing equations. Their values are listed in Table S2.

By adding a data loss term to Eq. 21, we can construct a hybrid training approach that uses both existing data and PDEs for training \mathbf{S}_ϕ . However, we show model performance under the end-member condition where no training data is available; thus, \mathbf{S}_ϕ here is a purely physics informed model without using any synthesized training data. As the loss function of \mathbf{S}_ϕ is data-free, the only pre-training computation needed are the random input thermal field T . Here, we use the random field with an exponential covariance kernel:

$$K(x, x') = \exp \left(-\frac{|x - x'|}{2l} \right) \quad (22)$$

whose variogram has a broad effective range of $|x - x'|$ (a long tail in its variogram function) compared with other common covariance models used in geostatistics, such as Gaussian or

spherical kernels (Webster & Oliver 2007; Müller et al. 2022). We utilize this property to incorporate structures of different wavelengths in our input so as to stimulate the operator learning effectively on all modes.

2.3.2 Forward and reverse convection neural operators

The convection neural operators $\mathbf{F}_\phi^{\pm n\Delta t}$ solve the forward ($+n\Delta t$) and reverse ($-n\Delta t$) convection problems within domain Ω with a fixed Rayleigh number described by Eq. 4 to 6. $\mathbf{F}_\phi^{+n\Delta t}$ approximates the mapping from a thermal state $T(\mathbf{x}, t)$ to both the Stokes velocity solution $\mathbf{u}(\mathbf{x}, t)$ and to another state that is $n\Delta t$ ahead in time, i.e., $T(\mathbf{x}, t + n\Delta t)$ (Fig. 2b), while $\mathbf{F}_\phi^{-n\Delta t}$ approximates the mapping from a thermal state $T(\mathbf{x}, t)$ to a previous state at $n\Delta t$ ago (Fig. 2c).

For the convection neural operators, either the forward or the reverse, their outputs and inputs are not explicitly connected by PDEs, rather a data-driven approach is used for training. An input-output training data pair is sampled from the thermal convection process (Eq. 4, 5) computed with `Underworld`. Due to the dissipative characteristic of $\mathbf{F}^{n\Delta t}$, the simplest way to create the training dataset spanning the input function space \mathcal{T} is to integrate the thermal states from some initial random fields. Here, the initial states of the training dataset are random thermal fields satisfying Dirichlet boundary conditions with a Gaussian covariance kernel:

$$K(x, x') = \exp\left(-\frac{(x - x')^2}{2l^2}\right) \quad (23)$$

Unlike the exponential covariance model (Eq. 22), the variogram of a Gaussian covariance model increases most rapidly near $|x - x'| = l$ which reflects the characteristic length scale within the thermal structure over which spatial correlation decays. Since the temperature at the upper boundary is fixed, such a characteristic correlation length scale will form an initial thermal boundary layer with thickness l . The thermal profile shows that this Gaussian boundary thermal gradient is similar to the error-function thermal gradient produced by conduction. We set l slightly larger than the boundary layer thickness at the steady state, in order to ensure that the overturn phase occurs quickly, incorporating abundant random movement, while avoiding the possible numerical instability brought on by large deviation from the distribution of T .

From each Gaussian initial thermal field, a temporal sequence of convection data can be generated by forward integration, and a large thermal convection dataset can thus be created

from multiple random initial states. By sampling data pairs with a specific time interval, we constructed the training dataset for forward convection neural operators. Reverse convection neural operators can be trained with exactly the same strategy by exchanging the previously sampled input-output pairs.

In addition to accelerating the forward computation, neural operators are also widely used in inverse problems (e.g., Li et al. 2020; Zou et al. 2025). When the forward calculation is performed as a sequential forward pass through the neural operator, a traceable computational graph is found with gradients between nodal values, thus the accumulated derivatives can be calculated using the chain rule, either from inside to outside (forward accumulation) or from outside to inside (reverse accumulation/backpropagation). This technique is known as automatic-differentiation and circumvents the need of solving adjoint equations (Griewank & Walther 2008), and can be easily performed in a highly-parallel way on GPUs. In fact the adjoint-state method is mathematically equivalent to automatic differentiation (Zhu et al. 2021). Hence, the gradient is now calculated using backpropagation and the derived gradient is more accurate compared to solving an adjoint equation, because it does not incorporate any numerical errors and can reach machine precision if the forward model is assumed as an accurate approximation to the ground-truth operator.

3 RESULTS

3.1 Physics-informed Stokes neural operator \mathbf{S}_ϕ

The Stokes equations (Eq. 4, 5) describes the mapping from the buoyancy field and viscosity structure to velocity and pressure, denoted as the Stokes operator \mathbf{S} . In its neural operator form \mathbf{S}_ϕ is trained with a purely physics-informed approach with loss function, L_S (Eq. 21). In this instance, we test the neural operator’s capability of a super-resolution prediction (Li et al. 2020): \mathbf{S}_ϕ is trained with random thermal inputs discretized on lower-resolution meshes (pre-trained on 65×65 and tuned on 129×129) and later evaluated on a finer one (257×257). First, we apply \mathbf{S}_ϕ to the temperature fields sampled from time window 1 (Fig. 1). For this forward convection example at $\text{Ra} = 10^7$, we found that it successfully resolves the flow even with high-frequency plume structure and achieves a L_2 relative error of $\sim 5\%$ compared to the velocity components solved by `Underworld`. Then, we also tested the accuracy of \mathbf{S}_ϕ by using three convecting thermal structures produced with $\text{Ra} = 10^5, 10^6, 10^7$, and different resolutions (65, 129, 257) as inputs (Fig. S2), and they performed equally well with their L_2 relative errors all around $\sim 5\%$ (Table 1). The point-wise errors in general align with the amplitudes of

velocity, showing some long wavelength features where the largest error occurs at the edges of convection cells, and diminishes within the thermally homogeneous regions. For \mathbf{u}_x , it occurs within the upper and lower thermal boundaries where the horizontal velocities reach the maximum; for \mathbf{u}_z , it occurs near the downwellings and upwellings. In general, the convection velocity patterns predicted by \mathbf{S}_ϕ are less vigorous with lower amplitudes. However, \mathbf{S}_ϕ seems to be capable of predicting accurate velocities within the thermal cores of the upwellings and downwellings. Often it is difficult to analytically explain the origin behind prediction errors of a neural network, however, the feature here, seems indicating that the Stokes neural operator resolves the local response of a thermal anomaly, but lacks the ability to accurately reproduce the spatial response in neighbor regions, compared with neural operators trained with data-driven methods, as to be detailed in next section. As there is usually a tradeoff between computational cost and solver accuracy, the moderate 5% prediction error could still make the physics informed Stokes neural operator usable for some forward, mantle dynamic computations, as considered in the Discussion.

As for the computational costs of formulating such a surrogate model, \mathbf{S}_ϕ is a purely physics informed neural operator that does not require any pre-training computational resource on solving the Stokes equations with traditional numerical methods to generate the training dataset. Rather, with random source term inputs, the training processes starts at no extra costs by evaluating several PDE losses from the output end, and the evaluation of PDE losses is much simpler than deriving the solution, especially when the system becomes non-linear and a iterative method is required to derive the solution. In other words, we achieved to make the entire workflow of training the Stokes neural operator and solving the forward problem in a 'CPU-free' manner. Besides, we utilized the super resolution feature of neural operators, that we trained \mathbf{S}_ϕ on a relatively coarse mesh, which further reduces the GPU expense. Hence, we suggest that for a one-step prediction model of which the underlying physics is already prescribed explicitly, the physics-informed approach could be the optimized strategy because of its efficiency.

3.2 Data-driven forward convection neural operators $\mathbf{F}_\phi^{+n\Delta t}$

We now demonstrate solving the forward convection problem using neural operators $\mathbf{F}_\phi^{+n\Delta t}$ with three different integration times (symbols listed in Table 2) across time window 1 in the computed convection sequence (Fig. 1), spanning about 14 transit times (t_{tr}), with a Rayleigh number of 10^7 . This test is carried out to evaluate the neural operators' accuracy and stability in modeling long term convection dynamics. Compared with the CFL limit in

Neural Operator	Ra	L_2 Relative Error	
		\mathbf{u}_x	\mathbf{u}_z
\mathbf{S}_ϕ	10^5	5.9%	5.2%
	10^6	5.3%	4.8%
	10^7	6.2%	5.5%

Table 1. Relative prediction errors of Stokes neural operator with convection patterns under different Rayleigh numbers.

traditional solvers, the integration time steps of forward convection neural operators are about hundred times larger. For $\mathbf{F}_{\phi_7}^{\pm 4}$ (the one with the largest time step), this contrast can reach ~ 300 times (Table 2, S3).

The operator $\mathbf{F}_\phi^{+n\Delta t}$ can be called recursively to compute time-dependent convection by integrating a thermal field forward to a next time step. It also has another output channel that predicts the current step velocity components. Comparisons between the output snapshots of thermal and velocity fields from forward computations using $\mathbf{F}_{\phi_7}^{+n\Delta t}$ and `Underworld` have been made (Fig. 3). In addition, diagnostic variables Nusselt number, Nu, and the maximum horizontal velocity, \mathbf{u}_{x0} , are also tracked within the time window for comparison.

All three forward convection neural operators with different integration time steps produce results that track almost equally well with the sequence computed by `Underworld`. The differences between the two methods remain small through the first transit time in terms of the internal fields and Nu and \mathbf{u}_{x0} . The relative error of neural operators' one-step prediction can be as low as 0.1% (Table 2). After $3 \sim 4$ transit times, the states computed by neural operators gradually diverge with those from `Underworld`, which is manifested in Nu and \mathbf{u}_{x0} trajectories. This phenomenon is expected and almost inevitable as the $\text{Ra} = 10^7$ system is highly non-linear, such that a small mismatch in the initial stages of the computation cause increasing deviations during the forward integration. Although the detailed convection patterns might deviate, both methods bring the convection process into a relatively steady state with two unit aspect ratio cells after 8 transit times, which indicates that the neural operators successfully learn the dissipative dynamics, reproducing an attractor near a steady state with two convection cells during long-term computation.

We also investigated how the neural operators' integration time step sizes influence the prediction accuracy. Although a clear trend of temperature prediction error with time step size is observed for $\mathbf{F}_{\phi_7}^{+n\Delta t}$, we found that a smaller time step does not guarantee a more precise

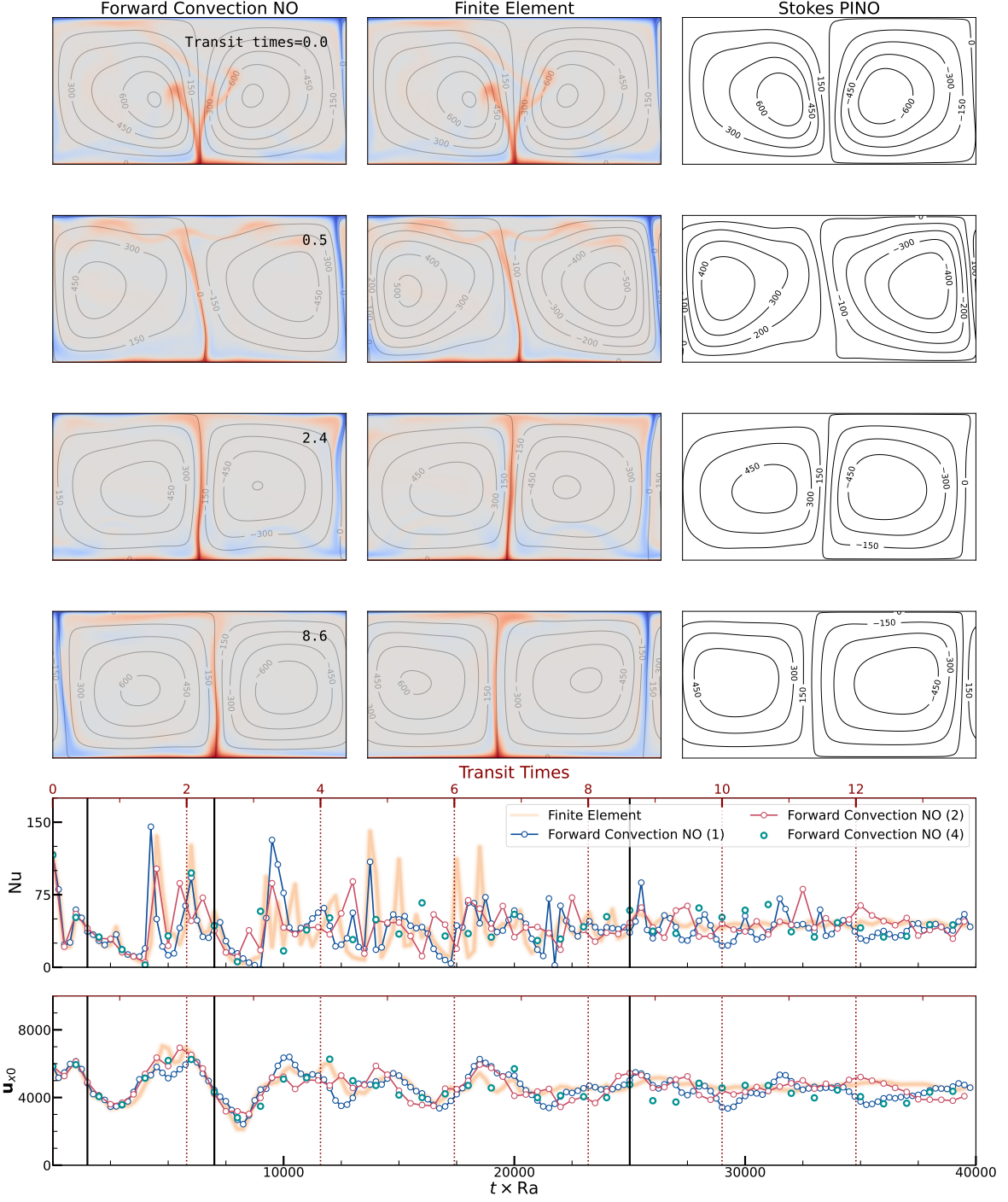


Figure 3. Comparisons between forward computations using $\mathbf{F}_{\phi_7}^{+n}$ and **Underworld**, $\text{Ra} = 10^7$. Row 1 to 4 shows the forward evolution snapshots of the systems. Column 1: temperature snapshots and velocity streamlines computed by $\mathbf{F}_{\phi_7}^{+1}$, system integrated by $\mathbf{F}_{\phi_7}^{+1}$; Column 2: temperature and velocity computed by **Underworld**, system integrated by **Underworld**; Column 3: velocity computed by \mathcal{S}_ϕ based on thermal fields integrated by **Underworld** as inputs. Row 5 and 6: Nu and \mathbf{u}_{x0} tracked in systems integrated with different methods. Black short bars indicate the instants where the snapshots within row 1 to 4 are chosen.

prediction when integrating a thermal field across a specific, long duration of time. The number of recursive steps is inversely proportional to the integration time, which results in a trade-off. By comparing against temperature predictions from **Underworld**, we find that for accuracy in long term forward integration, the three forward operators have a similar performance. On the other hand, as the velocity predictions are solutions of an instantaneous Stokes problem and thus independent of the forward integration time step size, its prediction error remains around 0.2% (Table 2). Nevertheless, circumventing the CFL constraint while using GPU computation, all three surrogate models accelerate the forward integration substantially with speedups proportional to the neural operators' time step size. For this problem, $\mathbf{F}_{\phi_7}^{+1}$, $\mathbf{F}_{\phi_7}^{+2}$, $\mathbf{F}_{\phi_7}^{+4}$ achieve speedups of around $5000\times$, $10000\times$, and $20000\times$ respectively, with a mesh of 257×257 (computational costs and comparisons listed in Table S6). The speedup factor could even scale up as the system size becomes larger. (See discussion and supplementary material for more details).

In addition, we have tested the neural operators' learnability under different Rayleigh numbers, 10^6 and 10^5 (Fig. S3 and S4). In lower Rayleigh number cases, the thermal convection is less unsteady and the underlying physics is easier for the neural operators to approximate. We find that for all the forward convection neural operators with different integration time steps tested (Table 2), predictions match and track the computation from **Underworld** more accurately as compared with the $\text{Ra} = 10^7$ case, and holds for tens of transit times. The performance of each forward convection neural operator is evaluated by inputting all of the ground-truth thermal states from the complete convection sequences (such as the one shown in Fig. 1) under three Rayleigh numbers to the corresponding neural operators and then calculated the relative L_2 error of each variable against the **Underworld** results. By averaging across the entire time window, we derived one-step prediction errors of all the output quantities (Table 2). They all remain small, implying that the forward convection neural operators are all well trained. Their accuracy in modeling the thermal convection through several transit times indicates their capability of becoming suitable surrogate forward models for inverse problems.

3.3 Thermal State Reconstruction

The outcomes from four different methods for the thermal state reconstruction (two backward integrations and two inverse methods) were computed and their performances were compared. A convection sequence of time window 3 (Fig. 1) computed with **Underworld** lasting for about 1 transit time is used as the ground-truth data against which the reconstructions are compared (Column 1, Fig. 4). To compute a realistic problem setup, our synthetic observables includes

Neural Operator	Ra	$n\Delta t$	Forward Model Single Step L_2 Relative Error		
			T	\mathbf{u}_x	\mathbf{u}_z
$\mathbf{F}_{\phi_5}^{+1}$	10^5	2.5×10^{-3}	3.8%	0.1%	0.1%
$\mathbf{F}_{\phi_6}^{+1}$	10^6	2.5×10^{-4}	0.7%	1.4%	0.1%
$\mathbf{F}_{\phi_7}^{\pm 1}$	10^7	2.5×10^{-5}	0.1%	0.3%	0.1%
$\mathbf{F}_{\phi_5}^{+2}$	10^5	5×10^{-3}	5.3%	0.1%	0.1%
$\mathbf{F}_{\phi_6}^{+2}$	10^6	5×10^{-4}	1.4%	1.3%	0.1%
$\mathbf{F}_{\phi_7}^{\pm 2}$	10^7	5×10^{-5}	0.3%	0.2%	0.1%
$\mathbf{F}_{\phi_5}^{+4}$	10^5	1×10^{-2}	4.6%	0.2%	0.1%
$\mathbf{F}_{\phi_6}^{+4}$	10^6	1×10^{-3}	2.8%	1.1%	0.1%
$\mathbf{F}_{\phi_7}^{\pm 4}$	10^7	1×10^{-3}	0.9%	0.4%	0.1%

Table 2. The symbols of forward (+) and reverse (−) convection neural operators, their integration times under different Rayleigh numbers, and one-step prediction error levels of forward convection neural operators.

the terminal thermal state and horizontal velocities on the upper surface as a function of time (Column 6, Fig. 4). Two backward integrations reverse convection directly from the terminal thermal state without utilizing the surface velocity data. As for the two inverse methods, we first incorporate observations from the terminal thermal state only, which takes the identical information as the direct methods; separate joint inversion is conducted while also using surface velocity observations. The reconstruction target is the initial thermal state (Fig. 4 and 5a). When evaluating the robustness of each method, ultimately for geophysical inversion, we consider a second experiment where the observations are polluted with noise (Fig. 6 and 5b).

The evolution in time window 3 starts from an initial state where there exists one upwelling and one downwelling plume spanning the domain. The system is not yet in a steady convective state (Fig. 1) which can be gleaned from the initial temperature field with several boundary layer instabilities. Forward in time, these thermal instabilities grow at the thermal boundary layers, velocities increase, and growing plumes merge into the existing larger ones (Column 1, Fig. 4, dynamics studied in detail in earlier literature, Hansen & Ebel (1988)). The surface velocity profile notably changes during the process, where the amplitude of convergence and divergence increases as new thermal structures mature; the imprints of those newly initiated structures are clearly recorded by the surface velocity profiles (Column 6, Fig. 4). Moreover,

the non-stationarity of the convection is evident in the final complex thermal structures, with plumes bent from the vertical and with distinct changes in plume width as a function of depth. Such complexity in the thermal structure retains information on the earlier time-dependence of the flow which we now attempt to recover.

We begin with the direct method of reversing the direction of buoyancy. Through backwards integration in time with reverse buoyancy and allowing diffusion to operate normally backwards in time (Eq. 8, 9, and 11) (Column 2, Fig. 4) a crude recovery is achieved. In this case, the thermal structures are advected back to the thermal boundary layers, rather than recovering the previous structures evident from the signals preserved in the current state. The consequence is that the reconstructed thermal state eventually becomes homogeneous with thick diffusive boundary layers and this method only recovers structures to less than $t = -0.34t_{tr}$, confirming earlier results (Conrad & Gurnis 2003; Ismail-Zadeh et al. 2004).

The second direct method integrates backward using the reverse convection neural operator (Column 3, Fig. 4). Compared with reverse buoyancy integration, the reverse convection neural operator not only recovers the dominant thermal structures with the correct amplitudes, but also recovers structure that subsequently underwent substantial diffusion. At $t = -0.34t_{tr}$, although we find that both methods reconstruct the merging of the downwelling on the right side of the box, only the reverse convection neural operator clearly recovers the downwelling on the left side, which had dissipated by the current state. By reversing buoyancy only, the vague signals of this mostly vanished structure are substantially smoothed. The fundamental difference between the two methods is that the reverse convection neural operator learns the anti-diffusion operator $-\nabla^2$, while by reversing buoyancy only, diffusion is over estimated during the backward integration. Consequently, the reverse convection neural operator is able to reconstruct further backwards in time. In contrast to the forward operator, we observe that the integration time step size of the reverse operator has a large influence on the accuracy of the recovered temperature across a specific long duration of time; for example, $\mathbf{F}_{\phi_7}^{-4}$ (column 3, Fig. 4) with the largest integration time step outperforms the others with smaller ones (Fig. 5). As $\mathbf{F}_{\phi_7}^{-4}$ has such a large step size, the reconstruction does not exactly match the ground truth steps shown, and consequently we integrate forward in time using forward convection neural operators between the check points to display a complete snapshot sequence in Fig. 4.

The inversion to reconstruct the initial state constrained only by the terminal temperature field is explored next (Column 4, Fig. 4). Compared with direct methods, the inversion recovers a convection pattern further back in time with quite realistic cold downwellings and warm

plumes in the interior compared with direct methods. However, thermal structures recovered before $t = -0.52t_{tr}$ appear to be non-physical with strong cold halos characterized by strong gradients around hot plumes and vice-versa, which lead to an incorrect evolutionary path. One possibility is that the optimization becomes trapped in non-physical, local minima by this time.

Finally, we utilized the information from both the terminal thermal state and surface velocity profiles in a joint inversion (Column 5, Fig. 4). We find that this approach outperforms all others by successfully reconstructing almost all thermal structures that once existed within the time window, including the merging of plumes, and the onset of instabilities. Particularly, the entire life cycle of the downwelling on the left side of the box is recovered. In addition, the reconstruction resolves the three upwellings that existed prior to their merger. The thermal field recovered at $t = -1.03t_{tr}$ (over one transit time) by joint inversion is still informative and contains the correct long wavelength structure compared with the ground truth. The initial state recovered by joint inversion leads to an evolutionary sequence that matches both the terminal states and the surface velocity profiles well (Column 6, Fig. 4).

Defined sequentially on the time axis, the chronological data stabilizes the inversion backward in time, improves the accuracy of inversion, avoids the optimization from being trapped into non-physical or local minima, and extends the time span for successful backward integrations. The influence of surface velocity can be seen in reconstructed thermal fields in which we find that the downwelling structures and the upper thermal boundary are better resolved than the upwellings and the lower thermal boundary. Essentially, the velocity data provides more constraints to shallower structure and this is evident from the sensitivity kernel of surface horizontal velocity to the underlying thermal field (Fig. S5). Nevertheless, the deeper structure is also substantially better constrained with surface velocities compared to inversions without as the deeper structure is strongly controlled by the shallow structure (e.g. downwellings control the locations of plume instability, Tan et al. (2002)). Comparing reconstructions using inversion with and without surface velocity, we find that without velocity the locations of surface convergent are not accurate and the reconstructed initial state can only be recovered for a short period backwards in time ($t \sim -0.34t_{tr}$); note that the fit to surface velocity is also poor if it is not used as a constraint (Column 6, Fig. 4).

Quantifying the correlation coefficient (see supplementary material) between reconstructed and ground truth thermal fields, we find that the error increases backwards in time with the joint inversion leading to the most robust recovery, followed by the reverse convection neural operator, the inversion by the terminal state, and lastly the reverse buoyancy (Fig. 5a). This

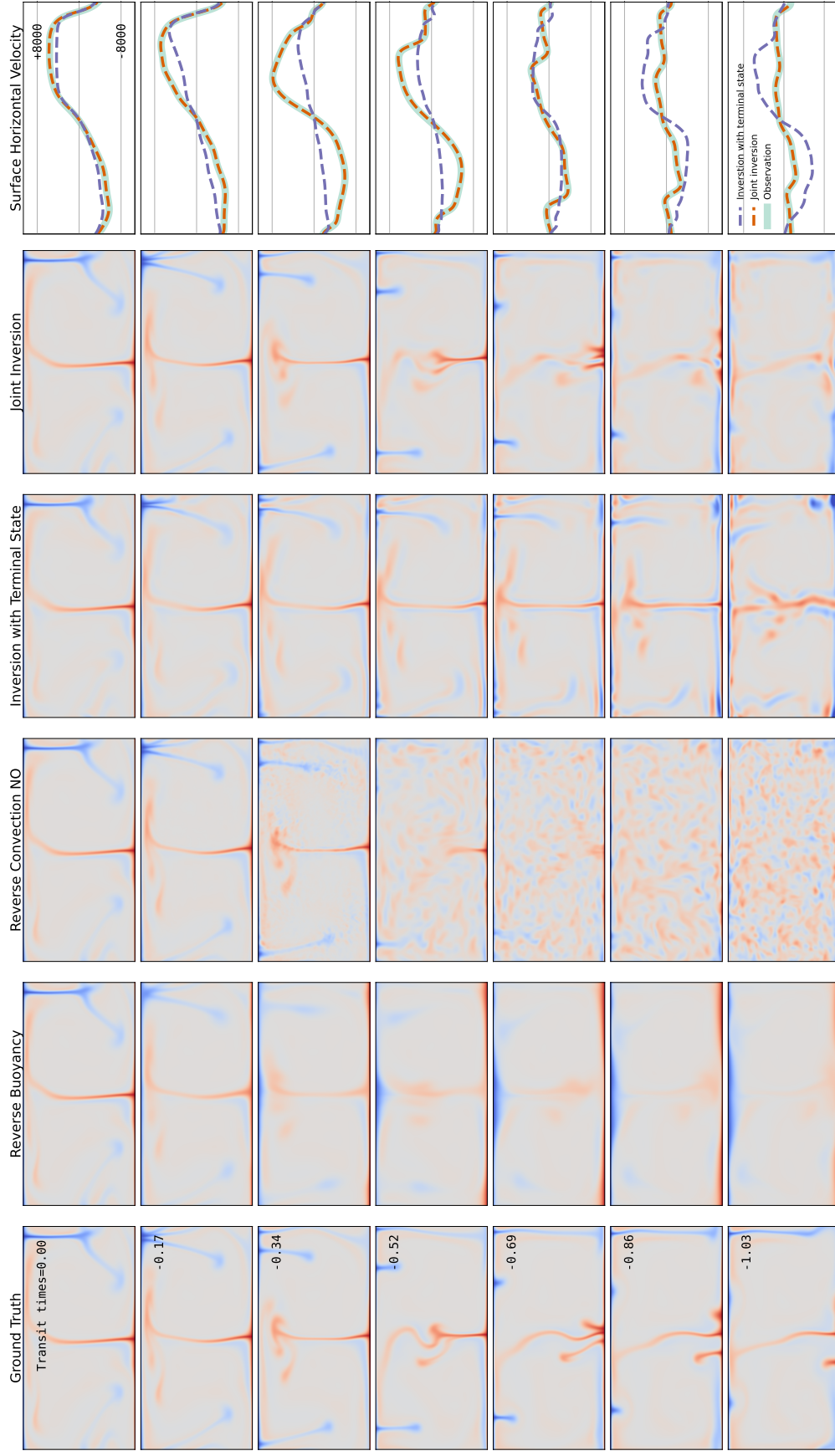


Figure 4. Reconstruction performances of different methods. Reversal time steps shown by row (from top to bottom backwards in time). Column 1: A ground-truth thermal convection sequence within time window 3 computed by `Underworld` forward in time from bottom to top; Column 2-5: Reconstruction with: reverse buoyancy; reverse convection operator; inversion with terminal state only; joint inversion; Column 6: Synthesized observations (clean), where the background in the top row shows the observed terminal thermal field, and the green curves represent the observed surface horizontal velocity profiles at each time step. The blue and red curves are the predicted surface velocities by two inversion methods.

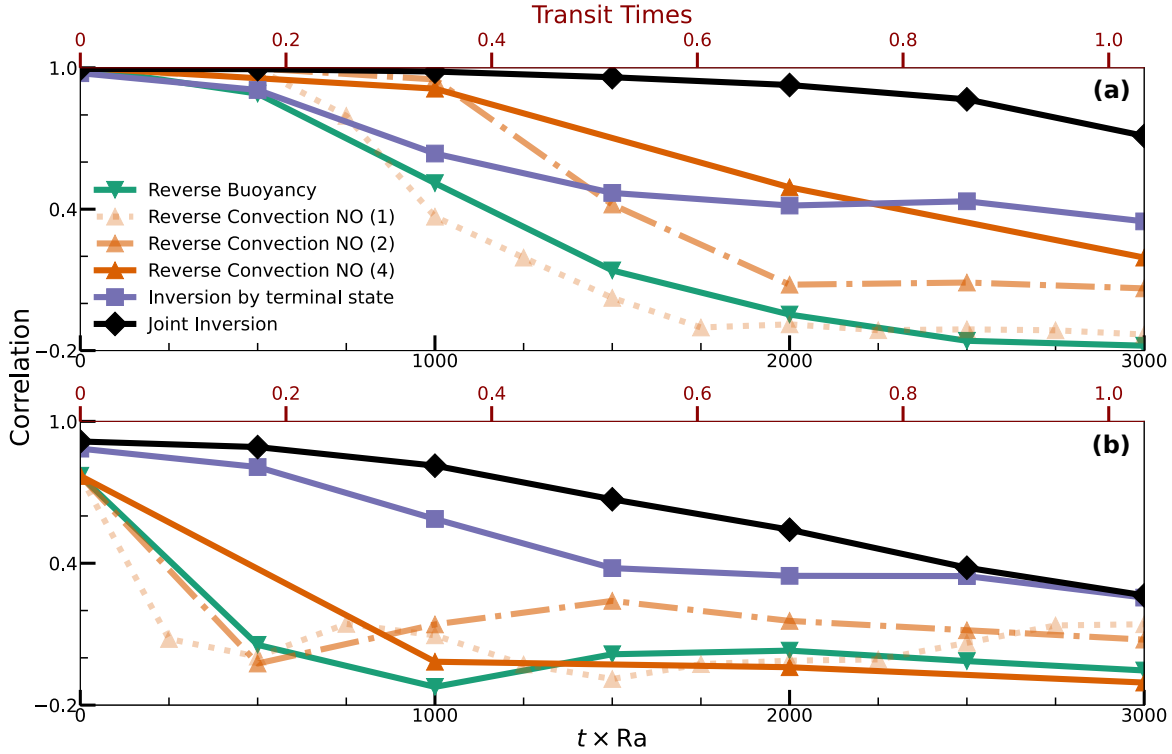


Figure 5. Correlation coefficient of reconstructed thermal fields with ground-truth fields versus backwards time. Colored lines denote different reconstruction methods. (a) Reconstruction with synthesized observations (no noise); (b) Reconstruction with synthesized observations polluted with 5% pink noise.

pattern generally holds most of the time. However, the performance of the reverse convection operator is better in some cases such as in time window 2 when smaller wavelength convection cells move laterally; with this time-dependence, the operator $\mathbf{F}_{\phi_7}^{-4}$ reconstructs the thermal state backwards over one transit time, and even outperforms the joint inversion approach in accuracy (Fig. S8).

Geophysical observations are noisy and so to explore the role of uncertainty on our four methods, we now compute thermal state reconstructions with the same methods but with observations polluted with 5% pink noise (Row 1, Column 2 and 3, Fig. 6). Compared with the previous results, large differences emerge in the reconstructions after adding the noise. The two direct methods, reverse buoyancy and the reverse convection neural operator fail to reconstruct even for short periods backward in time, although for different reasons. For the reverse buoyancy method, the pink noise in the terminal thermal state is interpreted as different short and long wavelengths features, in which the long wavelength ones especially cause substantial deviations in the flow upon reversal (Column 2, Fig. 6). As the reverse convection operator is an approximation to the ill-posed diffusion operator, it is quite sensitive

to noise, which is quickly amplified during backwards integration, and the output becomes unstable within just a single step backward (Column 3, Fig. 6).

In contrast, the inverse approaches remain robust and can provide informative reconstructions even in the presence of noise when sufficient constraints are used in the time domain. When using only the terminal state as a constraint, realistic plume structures and some down-wellings can be reconstructed to about $t = -0.34t_{tr}$ (Column 4, Fig. 6)—further back than the direct methods—but still less stable in comparison to the ideal case without noise. Many thermal structures cannot be reconstructed further back than this. However, when the surface velocity data is added in a joint inversion, the thermal state can be reconstructed back to $t = -0.86t_{tr}$ (Column 5, Fig. 6). Prior to this instant, the thermal structures become immersed in high frequency variations resulting from the noised terminal state thermal field. Compared with the terminal thermal state produced by the joint inversion, we find without surface velocity constraints, the upwelling plumes in the upper 3/4 of the domain at terminal state cannot be fully recovered. In other words, the addition of the time-constraints helps to “clean” the reconstruction from the structures that would be otherwise buried in noise. The correlations between reconstructions and ground truth in time verify the robustness of the joint inversion approach in the presence of noisy data (Fig. 5b).

4 DISCUSSION

We introduced three neural operators and examined their ability to learn aspects of mantle convection: (1) The Stokes neural operator \mathbf{S}_ϕ approximates the Stokes equations and maps temperature to velocity and pressure; (2) the forward convection neural operator $\mathbf{F}_\phi^{+n\Delta t}$; and (3) the reverse convection neural operator $\mathbf{F}_\phi^{-n\Delta t}$. The three neural operators have similar architecture, but differ in terms of prior information known of them, training strategy, well-posedness, and the degree to which they can improve computational efficiency, especially for inverse problems. The convection neural operators were then used within and compared against different methods for thermal state reconstructions including inverse models that use different data types.

We started with the Stokes neural operator with prior knowledge from the underlying conservation equations. Trained by known physical laws, this physics-informed approach has the lowest pre-training expense with random inputs without invoking expensive numerical solves; in contrast, numerical solves of Stokes for training dataset creation would contribute substantially to computational cost. The limitation of our physics informed approach is the difficulty of achieving the same precision for \mathbf{S}_ϕ as the data driven method (velocity channels

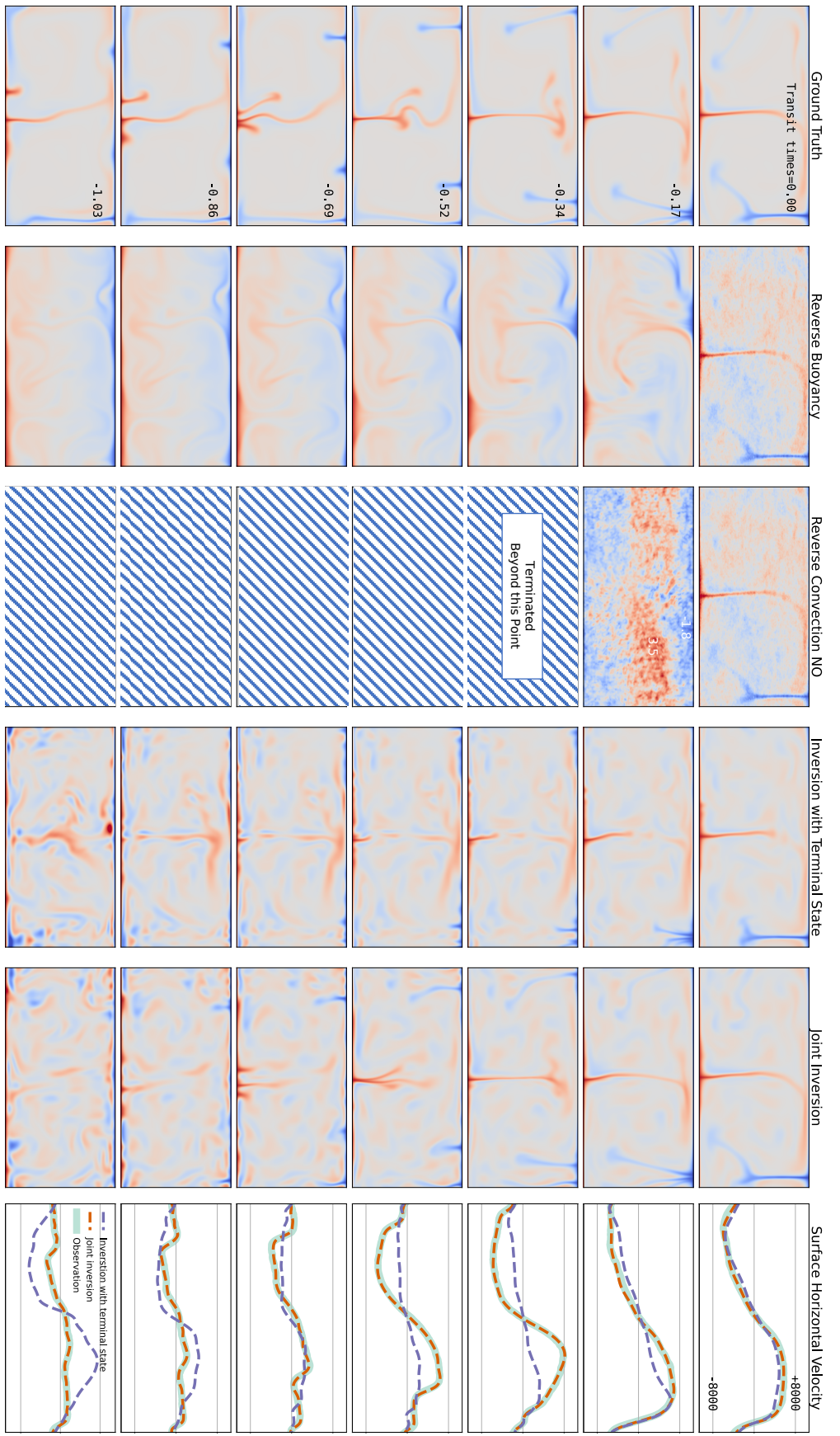


Figure 6. Reconstruction performances of different methods. Reversal time steps shown by row (from top to bottom backwards in time).

Column 1: A ground-truth thermal convection patterns within time window 3 computed by Underworld forward in time from bottom to top; Column 2-5: Reconstruction with: reverse buoyancy; reverse convection operator; inversion with terminal state only; joint inversion; ; Column 6: Observations (polluted), where the background in the top row shows the observed terminal thermal field, and the green curves represent the observed surface horizontal velocity profiles at each time step. The blue and red curves are the predicted surface velocities by two inversion methods.

of forward convection neural operators). Recall that our forward convection neural operators also output the Stokes velocities of the input thermal field, with a relative error around 0.1%. In contrast, the relative error from \mathbf{S}_ϕ is around 5%. The discrepancy could be caused by a physics informed loss function which is stiff, as well as its gradients. In the physics informed approach the loss function is composed of competing terms (Eq. 21), while for the data driven one, the loss function is simpler, in form of $L = \|T_{pred} - T_{true}\|_2 + \|\mathbf{u}_{pred} - \mathbf{u}_{true}\|_2$. Lacking explicit supervision from data, the neural operator has to be self-guided towards the optimized state by the dynamically competing components in the loss, which is substantially more difficult for the optimization (Wang et al. 2022). Thus, we encounter a trade-off between pre-training cost and prediction precision.

The Stokes neural operator works for instantaneous geodynamic solves such as computing surface kinematics, dynamic topography, state of stress, etc. As those output quantities can be directly acquired, they can be used as constraints to invert for hidden states of the mantle. In addition, the Stokes equation can take in more mantle state variables including viscosity and chemical composition as inputs, as does the neural operator, and lead to more realistic and comprehensive inversions. Along these lines using traditional methods, such as for an inversion of the thermochemical state of the mantle (Forte et al. 1994; Forte 2007) or for its non-linear rheology (Hu et al. 2024) both from surface plate kinematics, Stokes neural operators could be an effective replacement, speeding up such inversions. One limitation, however, for such instantaneous geodynamic inversions would be for models that involve the gravity field. The 5% error in velocity leads to even higher errors for dynamic topography limiting accurate prediction of the geoid (which is a consequence of small differences between nearly equal, but opposite, contributions from driving buoyancy and boundary deflections (Hager et al. 1985) and requires topography to be computed at high accuracy). Although the 5% relative velocity prediction error of the neural Stokes is a moderate level of bias, it might cause a large deviation if called recursively to integrate a thermal system forward in time. The bias to the inversion result is contributed by an integration from both the model itself and the inaccuracies/uncertainties of observations, while the later could be much larger compared with the 5% model error. The model prediction error can be tolerated and the inversion could still remain informative with appropriate regularization. The Stokes neural operator might also be able to provide initial guesses for iterative numerical solvers on large scale, non-linear systems.

In contrast, the forward convection neural operator is an example of data-driven operator discovery and maps between two thermal states separated by a long time interval, substantially

greater than the CFL limit (potentially hundreds of times). Although we have some prior knowledge about this system and are able to solve the output from the input numerically, the two ends are not directly connected by a single set of equations. By transforming a process originally composed of multiple operators into a single neural one, computational efficiency is greatly improved. The consequence is that the model must be trained at substantial cost. Moreover, since thermal convection is an initial value problem, the forward operator must be called recursively, requiring a high level of accuracy for each step. Our computations show that with sufficient training data, $\mathbf{F}_\phi^{n\Delta t}$ achieves a high accuracy in modeling thermal convection for three to four transit times, roughly 150 to 200 Myrs for mantle convection.

Although all forward convection neural operators trained under different Rayleigh numbers achieve satisfactory accuracy in temperature prediction, we observed that the prediction error moderately increases as Rayleigh numbers decrease and could be caused by different integration time step. Within the range tested, there is almost no indication that the long term prediction error is increasing with time step size. However, we did not train an operator having an even larger step, because the step size ultimately determines the interval over which the inversion can use chronological observations. Consequently, there is a balance between the ability to assimilate the constraints along the time axis and the number of recursive steps. If the step length is too large, the inversion will only have loose chronological constraints, while if too small, the computation will become more expensive. In the limit of large numbers of recursive integration steps, more GPU memory will be consumed as the entire computational chain is stored to enable auto-differentiation. In some cases with large memory usage check points might have to be introduced during backward propagation. Hence, as a compromise we choose the neural operator with medium time step $\mathbf{F}_{\phi_7}^{+2}$ to carry out the inversion.

The direct neural operator model we put forward for mantle state reconstruction is the reverse convection neural operator. Analogous to the forward one, it is also an attempt of operator discovery from data, and can even be trained based on the identical dataset prepared for the forward operator. Hence, for each forward surrogate model, a twin reversed operator can be trained. Our result shows that the reverse convection neural operator can indeed learn the ill-posed reverse process and predict backwards directly within a finite time interval, which is a breakthrough compared with numerical methods. However, it still shows some instability, include: (1) The performance could vary significantly dependent on the input thermal profile. We observed that if the convection pattern is dominated by four convection cells rather than two, the backwards integration by reverse convection neural operator remains stable for over one transit time. (2) They remain sensitive to noise and cannot be directly used in a realistic

geophysical process with noisy observations. The most robust approach remains the inverse approach based on forward models. Nevertheless, if the input of the reverse operator lies precisely in the realistic function space, the backwards prediction is still feasible. After all, the significant efficiency of the direct formulation of a reverse operator is still appealing. We suggest that a denoise mapping from the observation to the true function space can be jointly used with the ill-posed neural operator. This pre-processing mapping on the observation can be parameterized by a neural network, or formulated by a simpler inverse problem, and its outputs, might not only be denoised, but can also be transformed into other physical quantities if the observable one cannot be directly tackled by neural operators. For example, in mantle state reconstruction, the thermal state of mantle is indicated by seismic velocities using tomography. A transformation from noised and partially observed seismic velocities to a realistic thermal structure can be realized by an inversion constrained by the Stokes equation and wave equations. The pre-processing mapping can probably not only make the usage of reverse operator possible, even if we are using an inversion approach, incorporating such a procedure would also facilitates the inversion workflow.

In addition to the learnability, accuracy, and speedup of surrogate models, key is whether it is worthwhile to make a transition from traditional numerical solvers to surrogate ones, as the cost of training, especially the generation of training data, is considerable. For the purely physics informed Stokes neural operator, we have shown its learning ability without any pre-training cost, and its potential in instantaneous mantle dynamics modeling and inversions. For data-driven convection neural operators, although such surrogate models can speedup the computation substantially, their reliance on the training dataset could cause a notable cost. To evaluate, one needs to consider the cost of the entire workflow. Compared with traditional ones, the neural operator workflow has the extra cost for training data preparation and training, in addition to forward and backward integrations. The optimized option is different depending on the application scenarios (evaluation details described in the supplementary material for the models with $\text{Ra} = 10^7$): If the problem is a forward model integrated over a moderate interval (such as several transit times), the training of a neural operator might not be worthwhile; in this case, the cost of generating the training data will likely already exceed that of the traditional methods. For time-dependent inversions such as thermal state reconstruction, numerous iterations are required for optimization, with each iteration containing a forward and backward integration. The significant speedup by forward convection neural operators in integrations would manifest itself in such instance. Take the 2-D reconstruction across one transit time as an example, we suggest that the total cost of the neural

operator workflow would be comparable with that of performing an inversion with traditional methods once. When multiple inversion trials are required, it will be far more efficient. In addition, as the computation speedup scales with problem size, the efficiency of neural operator based workflow would become more pronounced for larger scale problems (see supplementary material). The comparison indicates a strong prospect of neural operator's applications in time-dependent inverse problems.

In this study, we have focused on 2-D isoviscous thermal convection. The simplified model shares many features in common with mantle convection and we demonstrated how neural operators can play a role in accelerating computation and reducing workflow costs. Yet, simplifications limit the range of geophysical problems the current neural operator can tackle. Although they could be applicable for regional reconstructions, in order to move forward towards deciphering mantle evolutionary history under realistic plate tectonics, a non-linear viscosity within a spherical shell is necessary. The incorporation of a rheology law does not change the nature of the problem, but would increase the demand of generating training dataset and cost, as does the geometry. However, the development of neural operator architectures are rapidly unfolding with advances showing even better performance than the FNO with the capability of learning complex physics at high-resolution within irregular domains (Li et al. 2023; Bonev et al. 2023; Shi et al. 2025). Simultaneously, progress with GPU hardware is making the training and deployment of large neural operators more efficient. Although needing considerable computational resources, development of a 3-D neural operator for global convection is likely close at hand.

5 CONCLUSIONS

The utility of neural operators is demonstrated for two-dimensinal, bottom-heated, Rayleigh–Bernard thermal convection. The results are consistent with earlier studies and have demonstrated that surrogate models in the form of neural operators can have a lower computational complexity when applied to both forward and backward calculations. The Fourier neural operator was used as the basic machine learning architecture. Starting by learning the Stokes system, an operator that can be expressed explicitly by a set of partial differential equations, the neural operator learns to solve the primitive variables from temperature with a purely physics informed approach without any training data, substantially reducing the pre-training cost. The physics informed Stokes neural operator can be potentially used as surrogate models for instantaneous geodynamics modeling and inversions. The mapping between two thermal states separated by temporal intervals significantly exceeding the CFL condition is approxi-

mated by forward convection neural operators through a data-driven training strategy. This surrogate model substantially accelerates forward convection computations through reducing the number of recursive steps. Furthermore, by exchanging the sequence of training data-pairs, the ill-posed reverse convection operators are approximated. The reverse convection operators are not unstable on integration as are the traditional numerical methods, and are able to predict previous mantle states directly. Several methods for thermal state reconstruction were developed and compared, including an inversion based on the forward convection neural operator and auto-differentiation. The results demonstrate this inverse approach is an accurate and robust method for reconstructing past states especially in the presence of observational noise. When chronological surface observations (surface kinematics) are added into a joint inversion along with the terminal thermal state, the method outperforms all other approaches. The accuracy of neural operators shows that it is a reliable method for mantle convection computations back about three to four transit times, roughly 150 to 200 Myrs for mantle convection, or enough to resolving a long-term tectonic process and the underlying dynamics behind. We also found that for a mantle state reconstruction, the total cost of the neural operator based work flow, which is dominated by training, is roughly comparable to performing the inversion using traditional numerical methods once. The substantial speed up in both forward and reverse computations and their scaling with the system size shows the prospect of global scaled, mantle state reconstructions.

ACKNOWLEDGMENTS

Temporarily left blank

DATA AVAILABILITY

For the final version of the manuscript, we will make our training data and code available on Caltech Data, <https://data.caltech.edu/>.

REFERENCES

- Agarwal, S., Tosi, N., Kessel, P., Breuer, D., & Montavon, G., 2021. Deep learning for surrogate modeling of two-dimensional mantle convection, *Physical Review Fluids*, **6**(11), 113801.
- Agarwal, S., Bekar, A. C., Hüttig, C., Greenberg, D. S., & Tosi, N., 2025. Physics-based machine learning for mantle convection simulations, *arXiv preprint arXiv:2505.16041*.

Alkin, B., Fürst, A., Schmid, S., Gruber, L., Holzleitner, M., & Brandstetter, J., 2024. Universal physics transformers: A framework for efficiently scaling neural operators, *Advances in Neural Information Processing Systems*, **37**, 25152–25194.

Atkins, S., Valentine, A. P., Tackley, P. J., & Trampert, J., 2016. Using pattern recognition to infer parameters governing mantle convection, *Physics of the Earth and Planetary Interiors*, **257**, 171–186.

Azizzadenesheli, K., Kovachki, N., Li, Z., Liu-Schiaffini, M., Kossaifi, J., & Anandkumar, A., 2024. Neural operators for accelerating scientific simulations and design, *Nature Reviews Physics*, **6**(5), 320–328.

Becker, T. W. & Fuchs, L., 2023. Generation of Evolving Plate Boundaries and Toroidal Flow From Visco-Plastic Damage-Rheology Mantle Convection and Continents, *Geochemistry, Geophysics, Geosystems*, **24**(12), e2023GC011179.

Billen, M. I., 2008. Modeling the dynamics of subducting slabs, *Annu. Rev. Earth Planet. Sci.*, **36**(1), 325–356.

Bonev, B., Kurth, T., Hundt, C., Pathak, J., Baust, M., Kashinath, K., & Anandkumar, A., 2023. Spherical Fourier neural operators: Learning stable dynamics on the sphere.

Brooks, A. N. & Hughes, T. J., 1982. Streamline upwind/Petrov-Galerkin formulations for convection dominated flows with particular emphasis on the incompressible Navier-Stokes equations, *Computer Methods in Applied Mechanics and Engineering*, **32**(1-3), 199–259.

Bunge, H.-P., Hagelberg, C., & Travis, B., 2003. Mantle circulation models with variational data assimilation: inferring past mantle flow and structure from plate motion histories and seismic tomography, *Geophysical Journal International*, **152**(2), 280–301.

Christensen, U., 1984. Convection with pressure-and temperature-dependent non-Newtonian rheology, *Geophysical Journal International*, **77**(2), 343–384.

Conrad, C. P. & Gurnis, M., 2003. Seismic tomography, surface uplift, and the breakup of Gondwanaland: Integrating mantle convection backwards in time, *Geochemistry, Geophysics, Geosystems*, **4**(3).

Conrad, C. P. & Lithgow-Bertelloni, C., 2002. How mantle slabs drive plate tectonics, *Science*, **298**, 207–209, doi: 10.1126/science.1074161.

Courant, R., Friedrichs, K., & Lewy, H., 1928. Über die partiellen differenzengleichungen der mathematischen physik, *Mathematische annalen*, **100**(1), 32–74.

Davies, G. F., 1999. *Dynamic Earth: Plates Plumes and Mantle Convection*, Cambridge University Press, Cambridge.

Engebretson, D. C., Cox, A., & Gordon, R. G., 1985. Relative motions between oceanic and continental plates in the Pacific basin, *Geol. Soc. Am. Sp. Paper*, **205**, 1–59.

Ernst, W., 1988. Tectonic history of subduction zones inferred from retrograde blueschist PT paths, *Geology*, **16**(12), 1081–1084.

Forte, A., 2007. Constraints on seismic models from other disciplines – implications for mantle dynamics and composition, in *Treatise on Geophysics*, pp. 805–858, ed. Schubert, G., Elsevier, Amsterdam.

Forte, A. M., Woodward, R. L., & Dziewonski, A. M., 1994. Joint inversions of seismic and geodynamic data for models of three-dimensional mantle heterogeneity, *Journal of Geophysical Research: Solid Earth*, **99**(B11), 21857–21877.

Gerya, T., 2019. *Introduction to Numerical Geodynamic Modelling*, Cambridge University Press.

Goess, S., Agrusta, R., Van Hunen, J., & Garel, F., 2017. Subduction-transition zone interaction: A review, *Geosphere*, **13**(3), 644–664.

Griewank, A. & Walther, A., 2008. *Evaluating derivatives: principles and techniques of algorithmic differentiation*, SIAM.

Gurnis, M., 1993. Phanerozoic marine inundation of continents driven by dynamic topography above subducting slabs, *Nature*, **364**, 589–593.

Hager, B. H. & O'Connell, R. J., 1981. A simple global model of plate dynamics and mantle convection, *J. Geophys. Res.*, **86**, 4843–4867.

Hager, B. H., Clayton, R. W., Richards, M. A., Comer, R. P., & Dziewonski, A. M., 1985. Lower mantle heterogeneity, dynamic topography and the geoid, *Nature*, **313**, 541–545.

Hansen, U. & Ebel, A., 1988. Time-dependent thermal convection-a possible explanation for a multiscale flow in the earth's mantle, *Geophysical Journal International*, **94**(2), 181–191.

Harris, N. B., Pearce, J. A., & Tindle, A. G., 1986. Geochemical characteristics of collision-zone magmatism, *Geological Society, London, Special Publications*, **19**(1), 67–81.

Hu, J., Rudi, J., Gurnis, M., & Stadler, G., 2024. Constraining Earth's nonlinear mantle viscosity using plate-boundary resolving global inversions, *Proceedings of the National Academy of Sciences*.

Ismail-Zadeh, A., Schubert, G., Tsepelev, I., & Korotkii, A., 2004. Inverse problem of thermal convection: numerical approach and application to mantle plume restoration, *Physics of the Earth and Planetary Interiors*, **145**(1-4), 99–114.

Kingma, D. P. & Ba, J., 2014. Adam: A method for stochastic optimization, *arXiv preprint arXiv:1412.6980*.

Kirsch, A. et al., 2011. *An Introduction to the Mathematical Theory of Inverse Problems*, vol. 120, Springer.

Koelemeijer, P., Ritsema, J., Deuss, A., & Van Heijst, H.-J., 2016. Sp12rts: a degree-12 model of shear-and compressional-wave velocity for earth's mantle, *Geophysical Journal International*, **204**(2), 1024–1039.

Kossaifi, J., Kovachki, N., Azizzadenesheli, K., & Anandkumar, A., 2023. Multi-grid tensorized Fourier neural operator for high-resolution PDEs, *arXiv preprint arXiv:2310.00120*.

Kovachki, N., Li, Z., Liu, B., Azizzadenesheli, K., Bhattacharya, K., Stuart, A., & Anandkumar, A., 2023. Neural operator: Learning maps between function spaces with applications to pdes, *Journal*

of Machine Learning Research, **24**(89), 1–97.

LeCun, Y., Bottou, L., Bengio, Y., & Haffner, P., 2002. Gradient-based learning applied to document recognition, *Proceedings of the IEEE*, **86**(11), 2278–2324.

Li, D., Gurnis, M., & Stadler, G., 2017. Towards adjoint-based inversion of time-dependent mantle convection with nonlinear viscosity, *Geophysical Journal International*, **209**(1), 86–105.

Li, Z., Kovachki, N., Azizzadenesheli, K., Liu, B., Bhattacharya, K., Stuart, A., & Anandkumar, A., 2020. Fourier neural operator for parametric partial differential equations, *arXiv preprint arXiv:2010.08895*.

Li, Z., Zheng, H., Kovachki, N., Jin, D., Chen, H., Liu, B., Azizzadenesheli, K., & Anandkumar, A., 2021. Physics-informed neural operator for learning partial differential equations, *arXiv preprint arXiv:2111.03794*.

Li, Z., Kovachki, N., Choy, C., Li, B., Kossaifi, J., Otta, S., Nabian, M. A., Stadler, M., Hundt, C., Azizzadenesheli, K., et al., 2023. Geometry-informed neural operator for large-scale 3d pdes, *Advances in Neural Information Processing Systems*, **36**, 35836–35854.

Liu, L. & Gurnis, M., 2008. Simultaneous inversion of mantle properties and initial conditions using an adjoint of mantle convection, *Journal of Geophysical Research: Solid Earth*, **113**(B8).

Long, M. D. & Becker, T. W., 2010. Mantle dynamics and seismic anisotropy, *Earth and planetary science letters*, **297**(3-4), 341–354.

Lu, C., Grand, S. P., Lai, H., & Garnero, E. J., 2019. TX2019slab: A New P and S Tomography Model Incorporating Subducting Slabs, *Journal of Geophysical Research: Solid Earth*, **124**(11), 11549–11567.

Mansour, J., Giordani, J., Moresi, L., Beucher, R., Kaluza, O., Velic, M., Farrington, R., Quenette, S., & Beall, A., 2020. Underworld2: Python geodynamics modelling for desktop, HPC and cloud, *Journal of Open Source Software*, **5**(47), 1797.

Marwah, T., Pokle, A., Kolter, J. Z., Lipton, Z., Lu, J., & Risteski, A., 2023. Deep equilibrium based neural operators for steady-state pdes, *Advances in Neural Information Processing Systems*, **36**, 15716–15737.

Merdith, A. S., Williams, S. E., Collins, A. S., Tetley, M. G., Mulder, J. A., Blades, M. L., Young, A., Armistead, S. E., Cannon, J., Zahirovic, S., et al., 2021. Extending full-plate tectonic models into deep time: Linking the neoproterozoic and the phanerozoic, *Earth-Science Reviews*, **214**, 103477.

Moresi, L., Dufour, F., & Mühlhaus, H.-B., 2003. A lagrangian integration point finite element method for large deformation modeling of viscoelastic geomaterials, *Journal of computational physics*, **184**(2), 476–497.

Müller, S., Schüler, L., Zech, A., & Heße, F., 2022. GSTools v1. 3: a toolbox for geostatistical modelling in Python, *Geoscientific Model Development*, **15**(7), 3161–3182.

Parsons, B. & Daly, S., 1983. The relationship between surface topography, gravity anomalies, and temperature structure of convection, *J. Geophys. Res.*, **88**(B2), 1129–1144.

Raissi, M., Perdikaris, P., & Karniadakis, G. E., 2019. Physics-informed neural networks: A deep learning framework for solving forward and inverse problems involving nonlinear partial differential equations, *Journal of Computational physics*, **378**, 686–707.

Ribe, N. M., 1989. Seismic anisotropy and mantle flow, *Journal of Geophysical Research: Solid Earth*, **94**(B4), 4213–4223.

Ritsema, J., Deuss, A., Van Heijst, H., & Woodhouse, J., 2011. S40RTS: a degree-40 shear-velocity model for the mantle from new Rayleigh wave dispersion, teleseismic traveltimes and normal-mode splitting function measurements, *Geophysical Journal International*, **184**(3), 1223–1236.

Seton, M., Müller, R. D., Zahirovic, S., Gaina, C., Torsvik, T., Shephard, G., Talsma, A., Gurnis, M., Turner, M., Maus, S., et al., 2012. Global continental and ocean basin reconstructions since 200 ma, *Earth-Science Reviews*, **113**(3-4), 212–270.

Shahnas, M., Yuen, D., & Pysklywec, R., 2018. Inverse problems in geodynamics using machine learning algorithms, *Journal of Geophysical Research: Solid Earth*, **123**(1), 296–310.

Shi, Y., Ross, Z. E., Asimaki, D., & Azizzadenesheli, K., 2025. Mesh-informed neural operator: A transformer generative approach, *arXiv preprint arXiv:2506.16656*.

Spasojevic, S., Liu, L., & Gurnis, M., 2009. Adjoint models of mantle convection with seismic, plate motion and stratigraphic constraints: North America since the Late Cretaceous, *Geochem. Geophys. Geosyst.*, **10**, Q05W02.

Stadler, G., Gurnis, M., Burstedde, C., Wilcox, L. C., Alisic, L., & Ghattas, O., 2010. The dynamics of plate tectonics and mantle flow: From local to global scales, *science*, **329**(5995), 1033–1038.

Steinberger, B. & O'Connell, R. J., 1998. Advection of plumes in mantle flow: implications for hotspot motion, mantle viscosity and plume distribution, *Geophysical Journal International*, **132**(2), 412–434.

Straat, M., Markmann, T., & Hammer, B., 2025. Solving turbulent Rayleigh-Benard convection using Fourier neural operators, *arXiv preprint arXiv:2501.16209*.

Tan, E., Gurnis, M., & Han, L., 2002. Slabs in the lower mantle and their modulation of plume formation, *Geochem. Geophys. Geosyst.*, **3**(11), 1067.

Torsvik, T. H., Müller, R. D., Van der Voo, R., Steinberger, B., & Gaina, C., 2007. Global plate motion frames: toward a unified model, *Reviews of Geophysics*, **46**.

Van Heck, H. & Tackley, P., 2008. Planforms of self-consistently generated plates in 3d spherical geometry, *Geophysical Research Letters*, **35**(19).

Wang, S., Yu, X., & Perdikaris, P., 2022. When and why PINNs fail to train: A neural tangent kernel perspective, *Journal of Computational Physics*, **449**, 110768.

Webster, R. & Oliver, M. A., 2007. *Geostatistics for environmental scientists*, John Wiley & Sons.

Yang, Y., Gao, A. F., Castellanos, J. C., Ross, Z. E., Azizzadenesheli, K., & Clayton, R. W., 2021. Seismic wave propagation and inversion with neural operators, *The Seismic Record*, **1**(3), 126–134.

Zhang, N., Zhong, S., Leng, W., & Li, Z.-X., 2010. A model for the evolution of the earth's mantle

structure since the early paleozoic, *Journal of Geophysical Research: Solid Earth*, **115**(B6).

Zhong, S. & Gurnis, M., 1995. Mantle convection with plates and mobile, faulted plate margins, *Science*, **267**(5199), 838–843.

Zhong, S., Zuber, M. T., Moresi, L., & Gurnis, M., 2000. Role of temperature-dependent viscosity and surface plates in spherical shell models of mantle convection, *Journal of Geophysical Research: Solid Earth*, **105**(B5), 11063–11082.

Zhong, S., Zhang, N., Li, Z.-X., & Roberts, J. H., 2007. Supercontinent cycles, true polar wander, and very long-wavelength mantle convection, *Earth and Planetary Science Letters*, **261**(3-4), 551–564.

Zhu, W., Xu, K., Darve, E., & Beroza, G. C., 2021. A general approach to seismic inversion with automatic differentiation, *Computers & Geosciences*, **151**, 104751.

Zou, C., Azizzadenesheli, K., Ross, Z. E., & Clayton, R. W., 2024. Deep neural Helmholtz operators for 3-D elastic wave propagation and inversion, *Geophysical Journal International*, **239**(3), 1469–1484.

Zou, C., Ross, Z. E., Clayton, R. W., Lin, F.-C., & Azizzadenesheli, K., 2025. Ambient noise full waveform inversion with neural operators, *arXiv preprint arXiv:2503.15013*.

Supplementary Material

S1 NEURAL OPERATOR ARCHITECTURES

The detailed neural operator hyperparameters are defined in Table. S1.

S2 PDE LOSSES OF PHYSICS INFORMED STOKES NEURAL OPERATOR

PDE losses of the physics informed Stokes neural operator is evaluated using finite difference method on operator outputs, namely \mathbf{u} and p , and they are defined on the same uniform grid spanning the physical domain Ω . In other words, the derivatives of \mathbf{u} and p are calculated on a non-staggered grid, which contrasts with the more widely used staggered grid approach when solving the Stokes equation, where \mathbf{u} is defined on primary nodes while p is defined on subgrids (Gerya 2019). It allows for a more natural evaluation of the first derivative of p on the primary nodes, on which the second derivative of \mathbf{u} is defined. As the two terms need to be evaluated together in the momentum conservation equation (Eq. 2), the staggered approach would reach a better accuracy. In our non-staggered approach, the momentum loss L_M is still evaluated on the primary (operator output) nodes by calculating the central difference to p , and the continuity loss L_C is evaluated on sub-nodes (Fig. S1).

The continuity loss L_C evaluated on the sub-nodes is:

Table S1. The architectural hyperparameters of neural operators trained in this study.

Neural Operators	Modes [†]	Hidden Channels [†]	Number of FB [◊]	Lifting Ratio *	Projection Ratio *	Rank [◊]
$\mathbf{F}_{\phi_5}^{+n\Delta t}$	65	128	6	2	2	0.25
$\mathbf{F}_{\phi_6}^{+n\Delta t}$	129	128	6	2	2	0.1
$\mathbf{F}_{\phi_7}^{\pm n\Delta t}$	129	128	6	2	2	0.1
\mathbf{S}_{ϕ}	65	128	5	1	1	0.25

Notes: [†] FB hyperparameters; * MLP hyperparameters; [◊] TFNO hyperparameters.

$$\begin{aligned}
L_C = & \sum_{i=1}^{N_x-1} \sum_{j=1}^{N_z-1} \left(\frac{1}{4} (T_{i,j} + T_{i,j+1} + T_{i+1,j} + T_{i+1,j+1}) - 0.5 \right)^2 \times \\
& \left(\frac{\mathbf{u}_{x,i,j} + \mathbf{u}_{x,i,j+1} - \mathbf{u}_{x,i+1,j} - \mathbf{u}_{x,i+1,j+1}}{2\Delta x} + \frac{\mathbf{u}_{z,i,j} + \mathbf{u}_{z,i+1,j} - \mathbf{u}_{z,i,j+1} - \mathbf{u}_{z,i+1,j+1}}{2\Delta z} \right)^2 \\
& + \sum_{j=1}^{N_z-1} \left(\frac{1}{4} (T_{N_x,j} + T_{N_x,j+1} + T_{2,j} + T_{2,j+1}) - 0.5 \right)^2 \times \\
& \left(\frac{\mathbf{u}_{x,N_x,j} + \mathbf{u}_{x,N_x,j+1} - \mathbf{u}_{x,2,j} - \mathbf{u}_{x,2,j+1}}{2\Delta x} + \frac{\mathbf{u}_{z,N_x,j} + \mathbf{u}_{z,2,j} - \mathbf{u}_{z,N_x,j+1} - \mathbf{u}_{z,2,j+1}}{2\Delta z} \right)^2
\end{aligned} \tag{S1}$$

L_M can be decomposed into two parts, L_{Mx} and L_{Mz} on $e_{\mathbf{x}}$ and $e_{\mathbf{z}}$ directions respectively. They are evaluated on primary nodes:

$$\begin{aligned}
L_{Mx} = & \left\| \eta \left(\frac{\partial^2 \mathbf{u}_x}{\partial x^2} + \frac{\partial^2 \mathbf{u}_x}{\partial z^2} \right) - \frac{\partial p}{\partial x} \right\|_2^2 \\
= & \sum_{i=2}^{N_x-1} \sum_{j=2}^{N_z-1} \left(\eta \left(\frac{\mathbf{u}_{x,i+1,j} - \mathbf{u}_{x,i-1,j}}{\Delta x^2} + \frac{\mathbf{u}_{x,i,j+1} - \mathbf{u}_{x,i,j-1}}{\Delta z^2} \right) - \frac{p_{i+1,j} - p_{i-1,j}}{2\Delta x} \right)^2 \\
& + \sum_{j=2}^{N_z-1} \left(\eta \left(\frac{\mathbf{u}_{x,2,j} - \mathbf{u}_{x,N_x-1,j}}{\Delta x^2} + \frac{\mathbf{u}_{x,1,j+1} - \mathbf{u}_{x,1,j-1}}{\Delta z^2} \right) - \frac{p_{2,j} - p_{N_x-1,j}}{2\Delta x} \right)^2 \\
& + \sum_{j=2}^{N_z-1} \left(\eta \left(\frac{\mathbf{u}_{x,2,j} - \mathbf{u}_{x,N_x-1,j}}{\Delta x^2} + \frac{\mathbf{u}_{x,N_x,j+1} - \mathbf{u}_{x,N_x,j-1}}{\Delta z^2} \right) - \frac{p_{2,j} - p_{N_x-1,j}}{2\Delta x} \right)^2 \\
& + \sum_{i=2}^{N_x-1} \left(\eta \left(\frac{\mathbf{u}_{x,i+1,1} - \mathbf{u}_{x,i-1,1}}{\Delta x^2} + \frac{\mathbf{u}_{x,N_x,3} - \mathbf{u}_{x,N_x,1}}{\Delta z^2} \right) - \frac{p_{i+1,1} - p_{i-1,1}}{2\Delta x} \right)^2 \\
& + \sum_{i=2}^{N_x-1} \left(\eta \left(\frac{\mathbf{u}_{x,i+1,N_y} - \mathbf{u}_{x,i-1,N_y}}{\Delta x^2} + \frac{\mathbf{u}_{x,N_x,N_y} - \mathbf{u}_{x,N_x,N_y-2}}{\Delta z^2} \right) - \frac{p_{i+1,N_y} - p_{i-1,N_y}}{2\Delta x} \right)^2 \\
& + \left(\eta \left(\frac{\mathbf{u}_{x,2,1} - \mathbf{u}_{x,N_x-1,1}}{\Delta x^2} + \frac{\mathbf{u}_{x,1,3} - \mathbf{u}_{x,1,1}}{\Delta z^2} \right) - \frac{p_{2,1} - p_{N_x-2,1}}{2\Delta x} \right)^2 \\
& + \left(\eta \left(\frac{\mathbf{u}_{x,2,1} - \mathbf{u}_{x,N_x-1,1}}{\Delta x^2} + \frac{\mathbf{u}_{x,N_x,3} - \mathbf{u}_{x,N_x,1}}{\Delta z^2} \right) - \frac{p_{2,1} - p_{N_x-2,1}}{2\Delta x} \right)^2 \\
& + \left(\eta \left(\frac{\mathbf{u}_{x,2,N_y} - \mathbf{u}_{x,N_x-1,N_y}}{\Delta x^2} + \frac{\mathbf{u}_{x,1,N_y} - \mathbf{u}_{x,1,N_y-2}}{\Delta z^2} \right) - \frac{p_{2,N_y} - p_{N_x-1,N_y}}{2\Delta x} \right)^2 \\
& + \left(\eta \left(\frac{\mathbf{u}_{x,2,N_y} - \mathbf{u}_{x,N_x-1,N_y}}{\Delta x^2} + \frac{\mathbf{u}_{x,N_x,N_y} - \mathbf{u}_{x,N_x,N_y-2}}{\Delta z^2} \right) - \frac{p_{2,N_y} - p_{N_x-1,N_y}}{2\Delta x} \right)^2
\end{aligned} \tag{S2}$$

Training Phase	Input Resolution	β_C	β_{C_1}	β_{C_2}	β_M	β_B	β_u	β_p
Pre-training 1	65×65	$1/65$	0	1	1	$1/65^2$	$10^{-3.5}$	10^2
Pre-training 2	65×65	$100/65$	0	1	1	$1/65^2$	$10^{-3.5}$	10^2
Tuning	129×129	$1/129$	1	0	1	$1/129^2$	$10^{-3.5}$	10^2

Table S2. Weighting coefficients of PDE losses to train the physics informed Stokes neural operator

$$\begin{aligned}
 L_{Mz} = & \left\| \eta \left(\frac{\partial^2 \mathbf{u}_z}{\partial x^2} + \frac{\partial^2 \mathbf{u}_z}{\partial z^2} \right) - \frac{\partial p}{\partial z} - (T - 0.5) \right\|_2^2 \\
 = & \sum_{i=2}^{N_x-1} \sum_{j=2}^{N_z-1} \left(\eta \left(\frac{\mathbf{u}_{z,i+1,j} - \mathbf{u}_{z,i-1,j}}{\Delta x^2} + \frac{\mathbf{u}_{z,i,j+1} - \mathbf{u}_{z,i,j-1}}{\Delta z^2} \right) - \frac{p_{i,j+1} - p_{i,j-1}}{2\Delta z} - T_{i,j} + 0.5 \right)^2 \\
 & + \sum_{j=2}^{N_z-1} \left(\eta \left(\frac{\mathbf{u}_{z,2,j} - \mathbf{u}_{z,N_x-1,j}}{\Delta x^2} + \frac{\mathbf{u}_{z,1,j+1} - \mathbf{u}_{z,1,j-1}}{\Delta z^2} \right) - \frac{p_{1,j+1} - p_{1,j-1}}{2\Delta z} - T_{1,j} + 0.5 \right)^2 \\
 & + \sum_{j=2}^{N_z-1} \left(\eta \left(\frac{\mathbf{u}_{z,2,j} - \mathbf{u}_{z,N_x-1,j}}{\Delta x^2} + \frac{\mathbf{u}_{z,N_x,j+1} - \mathbf{u}_{z,N_x,j-1}}{\Delta z^2} \right) - \frac{p_{N_x,j+1} - p_{N_x,j-1}}{2\Delta z} - T_{N_x,j} + 0.5 \right)^2 \\
 & + \sum_{i=2}^{N_x-1} \left(\eta \left(\frac{\mathbf{u}_{z,i+1,1} - \mathbf{u}_{z,i-1,1}}{\Delta x^2} + \frac{\mathbf{u}_{z,N_x,3} - \mathbf{u}_{z,N_x,1}}{\Delta z^2} \right) - \frac{p_{i,2} - p_{i,1}}{\Delta z} - T_{i,1} + 0.5 \right)^2 \\
 & + \sum_{i=2}^{N_x-1} \left(\eta \left(\frac{\mathbf{u}_{z,i+1,N_y} - \mathbf{u}_{z,i-1,N_y}}{\Delta x^2} + \frac{\mathbf{u}_{z,N_x,N_y} - \mathbf{u}_{z,N_x,N_y-2}}{\Delta z^2} \right) - \frac{p_{i,N_y} - p_{i,N_y-1}}{\Delta z} - T_{i,N_z} + 0.5 \right)^2 \\
 & + \left(\eta \left(\frac{\mathbf{u}_{z,2,1} - \mathbf{u}_{z,N_x-1,1}}{\Delta x^2} + \frac{\mathbf{u}_{z,1,3} - \mathbf{u}_{z,1,1}}{\Delta z^2} \right) - \frac{p_{1,2} - p_{1,1}}{\Delta z} - T_{1,1} + 0.5 \right)^2 \\
 & + \left(\eta \left(\frac{\mathbf{u}_{z,2,1} - \mathbf{u}_{z,N_x-1,1}}{\Delta x^2} + \frac{\mathbf{u}_{z,N_x,3} - \mathbf{u}_{z,N_x,1}}{\Delta z^2} \right) - \frac{p_{N_x,2} - p_{N_x,1}}{\Delta z} - T_{N_x,1} + 0.5 \right)^2 \\
 & + \left(\eta \left(\frac{\mathbf{u}_{z,2,N_y} - \mathbf{u}_{z,N_x-1,N_y}}{\Delta x^2} + \frac{\mathbf{u}_{z,1,N_y} - \mathbf{u}_{z,1,N_y-2}}{\Delta z^2} \right) - \frac{p_{1,N_y} - p_{1,N_y-1}}{\Delta z} - T_{1,N_z} + 0.5 \right)^2 \\
 & + \left(\eta \left(\frac{\mathbf{u}_{z,2,N_y} - \mathbf{u}_{z,N_x-1,N_y}}{\Delta x^2} + \frac{\mathbf{u}_{z,N_x,N_y} - \mathbf{u}_{z,N_x,N_y-2}}{\Delta z^2} \right) - \frac{p_{N_x,N_y} - p_{N_x,N_y-1}}{\Delta z} - T_{N_x,N_z} + 0.5 \right)^2
 \end{aligned} \tag{S3}$$

$$L_M = L_{Mx} + L_{Mz} \tag{S4}$$

Fig. S2 shows the velocity predictions from \mathbf{S}_ϕ with inputs from convection patterns under different Rayleigh numbers ($10^5, 10^6, 10^7$), and different resolutions ($65 \times 65, 129 \times 129, 257 \times 257$), respectively. Table. S2 lists the weighting coefficients used to train \mathbf{S}_ϕ .

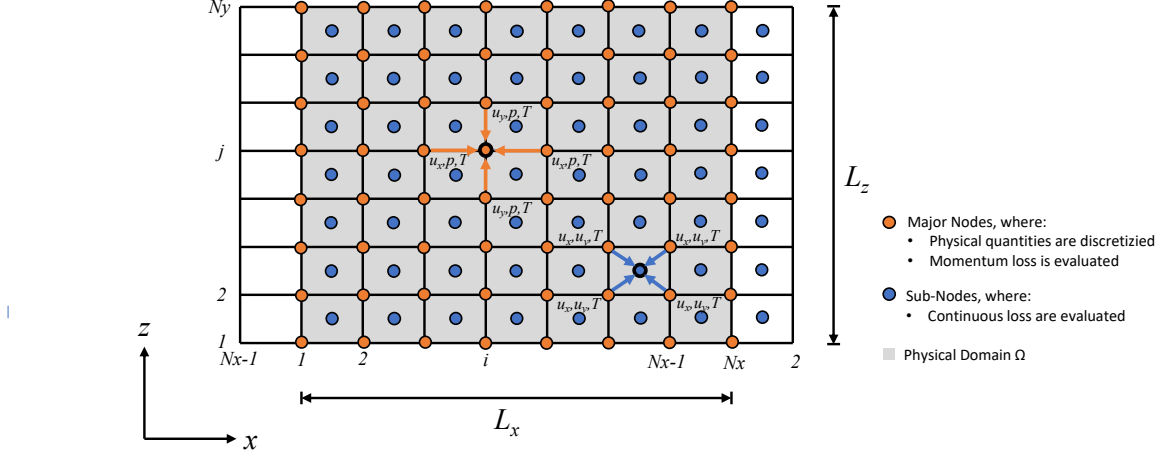


Figure S1. The evaluation method of PDE losses for the training of \mathbf{S}_ϕ . The gray shaded area shows the physical domain Ω . The orange dots show the primary nodes on which the physical quantities, T , \mathbf{u} , and p are discretized, and the momentum loss L_M is evaluated. The blue dots show the sub-nodes on which the continuity loss L_C is evaluated. Two dots circled with heavy boundaries show examples how the physical information from the neighbor nodes are utilized during the evaluation. Since two side boundaries are periodic, an extra column of sub-nodes are attached to the side of physical domain, in order to evaluate the continuity across the side boundaries.

S3 DATA-DRIVEN CONVECTION NEURAL OPERATORS

The integration time steps of data-driven convection neural operators are significantly larger than the CFL time steps with regards to convection patterns at specific Rayleigh numbers.

We tracked two variables: Nusselt number Nu , maximum horizontal velocity of the convection cell \mathbf{u}_{x0} , of convection in time window 1 computed by the forward convection neural operator and `Underworld` to evaluate the long term prediction stability and accuracy. Nu is given by

$$\text{Nu} = \frac{\int_{\Omega} \mathbf{u}_z T d\Omega + k(T_b - T_t)/D}{k(T_b - T_t)/D} \quad (\text{S5})$$

and \mathbf{u}_{x0} is calculated by searching for the largest velocity components in the domain.

Besides the example of $\text{Ra} = 10^7$ provided in the main text, we also present the examples

	Ra	10^5	10^6	10^7
CFL time step	2.12×10^{-5}	2.27×10^{-6}	2.5×10^{-7}	

Table S3. CFL time steps of steady convection patterns at different Rayleigh numbers.

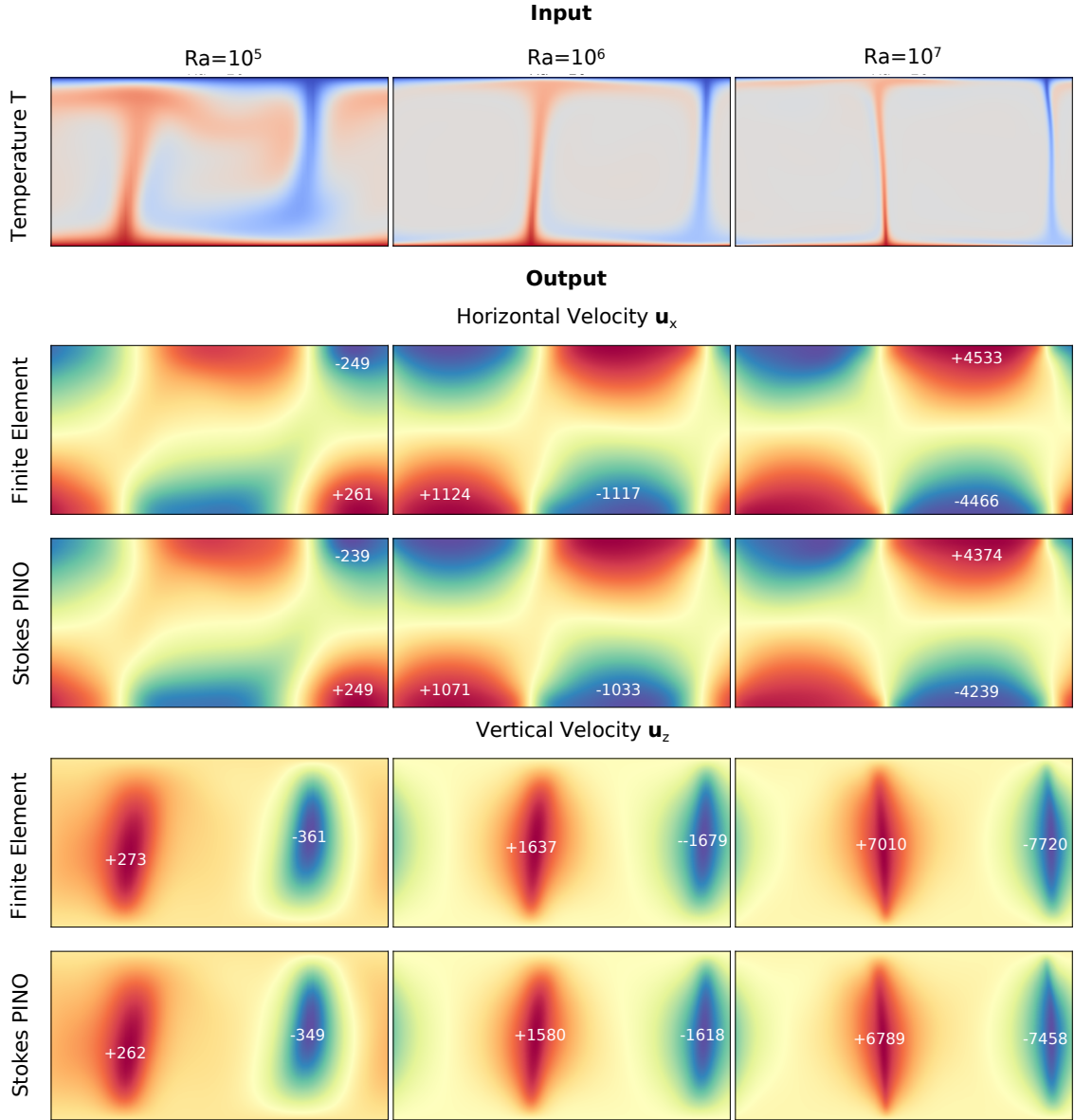


Figure S2. Row 1: the source terms (input temperature T); Row 2 and 3: solutions of \mathbf{u}_x from `Underworld` and \mathbf{S}_ϕ ; Row 5 and 6: solutions of \mathbf{u}_z from `Underworld` and \mathbf{S}_ϕ . The amplitudes of output velocity components are shown with numbers in white.

of convection modeling by forward convection neural operators with lower Rayleigh numbers, $\text{Ra} = 10^6$ and 10^5 (Fig. S3 and S4).

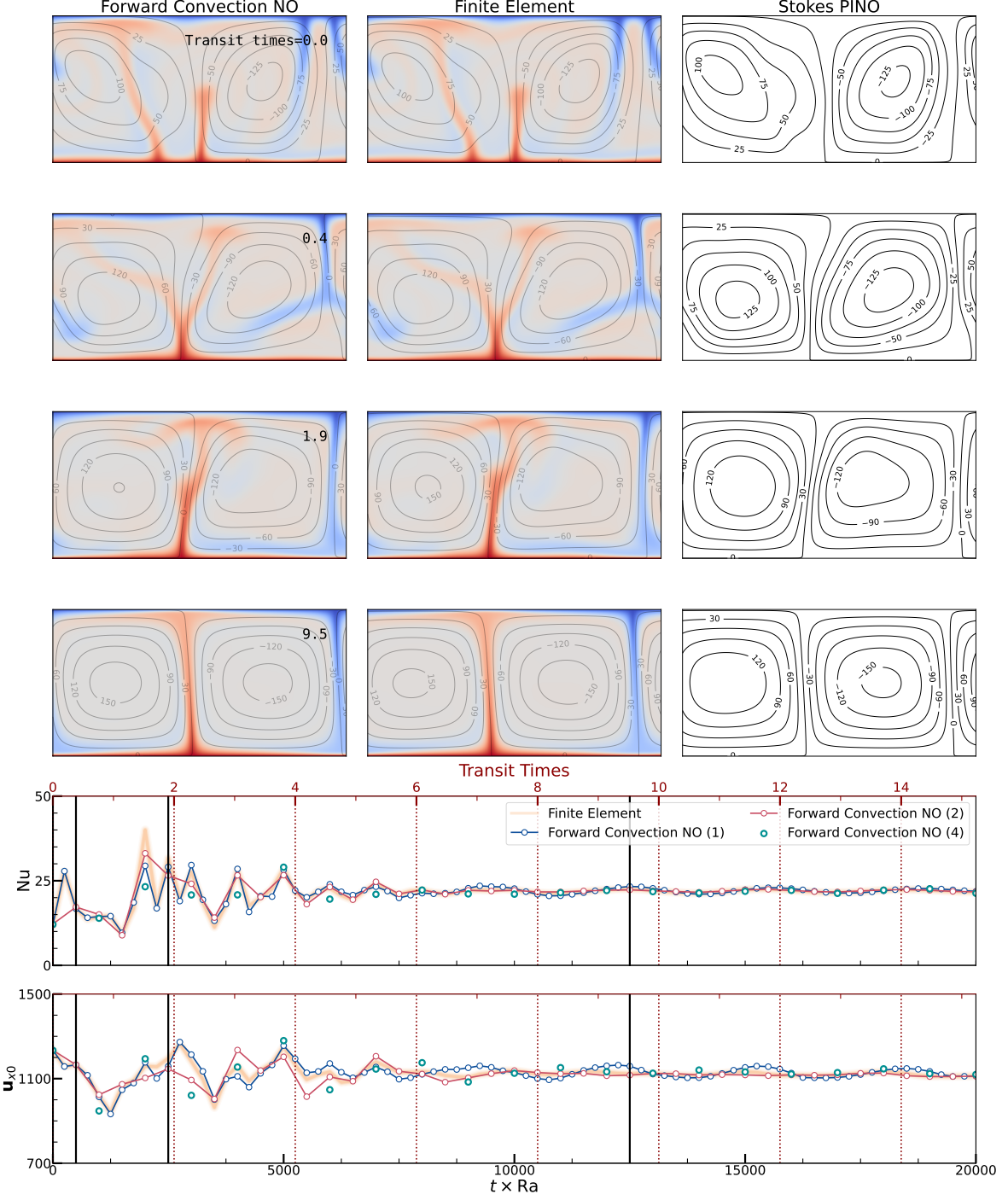


Figure S3. Comparisons between forward computations using $\mathbf{F}_{\phi_6}^{+n}$ and **Underworld**, $\text{Ra} = 10^6$. Row 1 to 4 shows the forward evolution snapshots of the systems. Column 1: temperature snapshots and velocity streamlines computed by $\mathbf{F}_{\phi_6}^{+1}$, system integrated by $\mathbf{F}_{\phi_6}^{+1}$; Column 2: temperature and velocity computed by **Underworld**, system integrated by **Underworld**; Column 3: velocity computed by \mathcal{S}_ϕ based on thermal fields integrated by **Underworld** as inputs. Row 5 and 6: Nu and \mathbf{u}_{x0} tracked in systems integrated with different methods. Black short bars indicate the instants where the snapshots within row 1 to 4 are chosen.

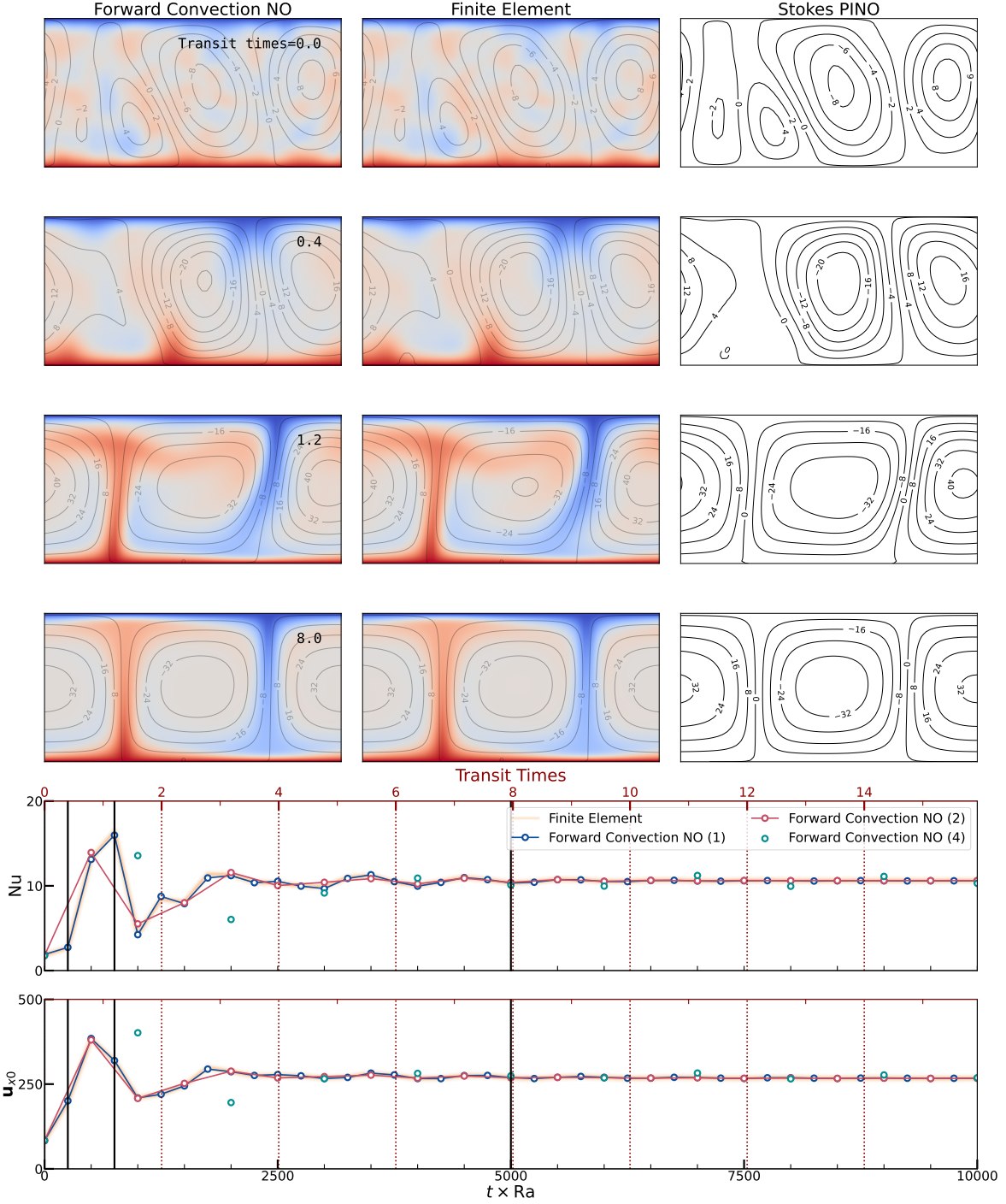


Figure S4. Comparisons between forward computations using $\mathbf{F}_{\phi_5}^{+n}$ and **Underworld**, $\text{Ra} = 10^5$. Row 1 to 4 shows the forward evolution snapshots of the systems. Column 1: temperature snapshots and velocity streamlines computed by $\mathbf{F}_{\phi_5}^{+1}$, system integrated by $\mathbf{F}_{\phi_5}^{+1}$; Column 2: temperature and velocity computed by **Underworld**, system integrated by **Underworld**; Column 3: velocity computed by \mathcal{S}_ϕ based on thermal fields integrated by **Underworld** as inputs. Row 5 and 6: Nu and \mathbf{u}_{x0} tracked in systems integrated with different methods. Black short bars indicate the instants where the snapshots within row 1 to 4 are chosen.

S4 SENSITIVITY KERNEL OF SURFACE HORIZONTAL VELOCITY

The neural operator approach that we use for solving the Stokes system, especially the surface kinematics in thermal state reconstruction, can be validated and placed within a traditional mathematical approach through the following scheme. As the viscosity is assumed to be constant, the Stokes system here formulates a linear mapping from temperature to velocity and pressure. Hence, the solution can be represented in terms of a convolution between its Green's function and the source term; the approach we lay out below is analogous to the approach used to compute dynamic topography and gravity anomalies from flow within a constant viscosity, Cartesian fluid layer as developed by Parsons & Daly (1983). The Green's function of the Stokes operator can not only be used to examine the accuracy of a numerically approximated operator (for example, a numerical solver, or a neural operator) by comparing its Green's function to the analytical solution, and can also be used to measure the sensitivity of surface velocity to temperature. This later use is of great importance to isolate the influence of surface kinematics in the thermal state reconstructions we introduced in this paper. We consider basal heated convection with periodic side walls between two isothermal boundaries. The sensitivity of surface horizontal velocity is determined by the depth $1 - z$ and horizontal wavelength $2\pi/k$ of the underlying thermal structure. Here, we prescribe the form of a Green's function as $\tilde{V}(k, z)$. We replace $\mathbf{u}(x, z)$ with the stream function $\psi(x, z)$:

$$\mathbf{u} = \left(-\frac{\partial\psi}{\partial z}, 0, \frac{\partial\psi}{\partial x} \right) \quad (\text{S6})$$

In such a case, the Stokes system is governed by the biharmonic equation:

$$\nabla^4\psi = \frac{\partial T}{\partial x} \quad (\text{S7})$$

By transferring ψ and T from spatial space (x, z) to (k, z) with the Fourier transformation in x direction, we have:

$$\hat{\psi}(k, z) = \frac{1}{\sqrt{2\pi}} \int_{-\infty}^{\infty} \psi(x, z) e^{-ikx} dx \quad (\text{S8})$$

$$\hat{T}(k, z) = \frac{1}{\sqrt{2\pi}} \int_{-\infty}^{\infty} T(x, z) e^{-ikx} dx \quad (\text{S9})$$

Then, the Stokes system becomes

$$\left(\frac{d^2}{dz^2} - k^2 \right)^2 \hat{\psi} = ik\text{Ra}\hat{T} \quad (\text{S10})$$

The solution to Eq. S10 is:

$$\hat{\psi}(k, z) = ik \int_0^1 \Psi(k, z, z') T(k, z') dz' \quad (\text{S11})$$

where $\Psi(k, z, z')$ is the fundamental solution, or Green's function, to Eq. S11. It is the solution to

$$\left(\frac{d^2}{dz^2} - k^2 \right)^2 \Psi = ik \text{Ra} \delta(z - z') \quad (\text{S12})$$

When the top and bottom boundaries are assumed to be free-slip (zero normal velocity and zero shear stress), $\Psi(k, z, z')$ is given by Parsons & Daly (1983)

$$\hat{\psi} = \begin{cases} A_1 \sinh k(1-z) + B_1 \cosh k(1-z) + C_1(1-z) \sinh k(1-z) + D_1(1-z) \cosh k(1-z), & z' \leq z \\ A_2 \sinh kz + B_2 \cosh kz + C_2 \sinh kz + D_2 \cosh kz, & z' > z \end{cases} \quad (\text{S13})$$

where:

$$A_1 = \frac{1}{2k^3 \sinh^2 k} (k(1-z') \sinh k \cosh kz' - k \sinh k(1-z') + \sinh k \sinh kz') \quad (\text{S14})$$

$$A_2 = \frac{1}{2k^3 \sinh^2 k} (kz' \sinh k \cosh k(1-z') - k \sinh kz' + \sinh k \sinh k(1-z')) \quad (\text{S15})$$

$$B_1 = B_2 = 0 \quad (\text{S16})$$

$$C_1 = C_2 = 0 \quad (\text{S17})$$

$$D_1 = -\frac{1}{2k^2 \sinh k} \sinh kz' \quad (\text{S18})$$

$$D_2 = -\frac{1}{2k^2 \sinh k} \sinh k(1-z') \quad (\text{S19})$$

From $\Psi(k, z, z')$ we obtain

$$\tilde{V}(k, z) = -\frac{\partial \Psi(k, z, 0)}{\partial z} \quad (\text{S20})$$

The depth dependence of \tilde{V} with a given wave number k , or $\tilde{V}_k(z)$, is shown for different wave numbers (Fig. S5), where we have chosen $k = \pi/D, 2\pi/D, 3\pi/D$, and $4\pi/D$. $\tilde{V}_k(z)$ equals to 0 on both top and bottom boundaries, and has a single peak value within the upper half of the domain, indicating the surface velocity's most sensitive depth of a given wavelength structure. The most sensitive depth can be seen to decrease as k becomes larger. By solving Eq. S12 with neural operators, we compute the neural operator's learned kernel, \tilde{V} (Fig. S5). Two

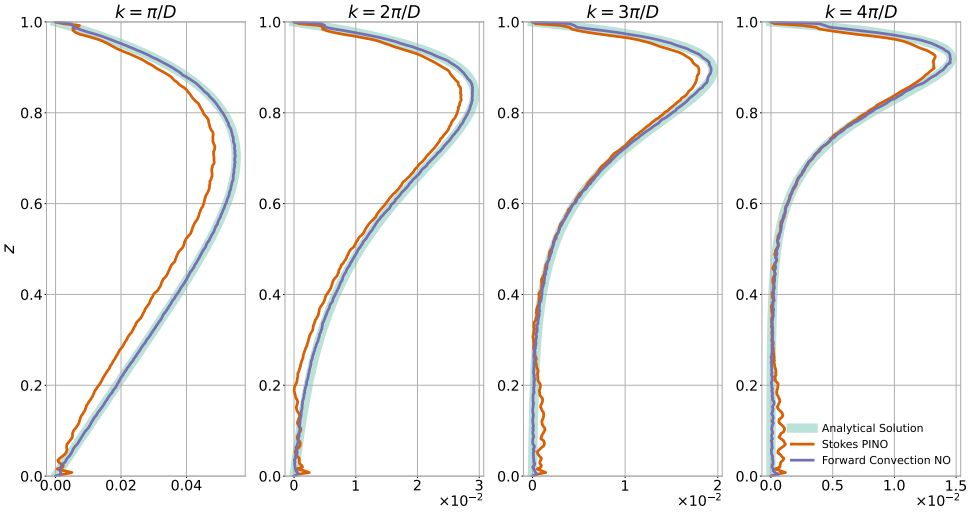


Figure S5. Green's functions of surface velocity to the thermal structure $\tilde{V}_k(z)$, shown by perturbation structures' wave numbers k in columns. Vertical axis z is the perturbation structures' burial depth and the horizontal axis denotes the amplitudes of the kernel. Neural operators' solutions from $\mathbf{F}_{\phi_7}^5$ and \mathbf{S}_ϕ are compared against the analytical solution Eq. S13.

kernels of the forward convection neural operator $\mathbf{F}_{\phi_7}^5$ and the Stokes neural operator \mathbf{S}_ϕ are given.

S5 OPTIMIZATION IN JOINT THERMAL STATE INVERSION

The weighting coefficients of Eq. 13 is listed in Table S4:

In the objective function Eq. 13, all the observations, including N surface horizontal velocity profiles and the terminal thermal state, are utilized when calculating the gradient, leading to a full gradient descent scheme. As for the inversion demonstrated in this study $N = 6$. In addition, we also tested optimizing with a stochastic gradient descent (SGD) approach. During each iteration, gradient is evaluated by a mini-batch containing a random subset of $N/3$ velocity profiles and the terminal thermal state to calculate the gradient. Mini-batch SGD produces a convergent misfit value around the same magnitude as results derived with

β_1	β_2	β_3	β_4
1.0	2.5×10^{-1}	1.0×10^{-5}	2.0×10^{-8}

Table S4. Weighting coefficients of the objective function.

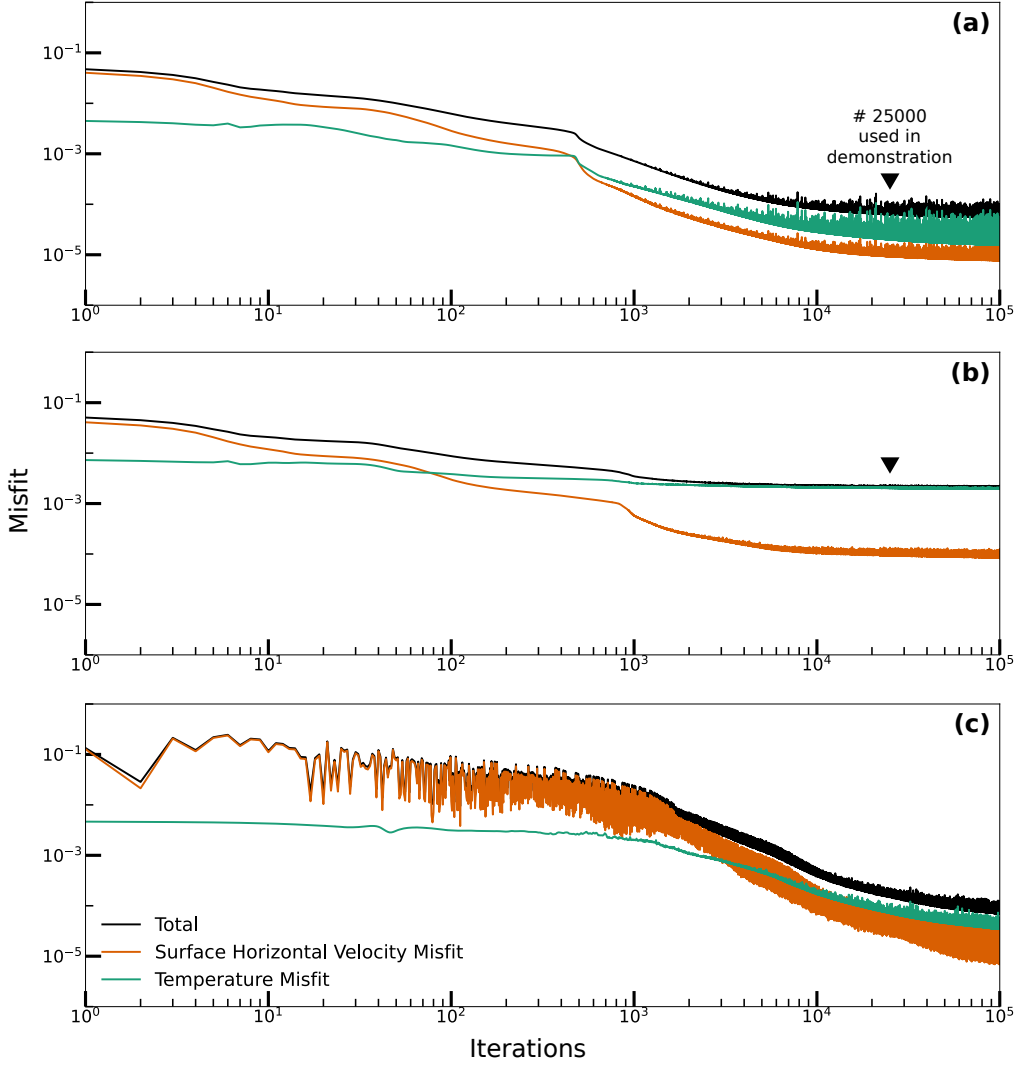


Figure S6. Optimization curves of the joint inversions, where the black lines indicate the values of the objective function Eq.13, and the colored lines indicate the misfit values to two observations. (a): Joint inversion; (b) Joint inversion with polluted synthesized observations; (c) Joint inversion using stochastic gradient descent. The triangles in (a)(b) denotes the 25000th optimization iteration, at which the optimization has converged and the results are used as demonstrations in Fig.4.

full gradient descent (Fig.S6c). However, due to reduction in both batch size and step size, it requires more iterations (about three times in our attempt compared with full gradient descent) to converge. Since the observation dataset volume $N + 1 = 7$ is not that large in our case, we adopted the simplest full gradient descent scheme in this study.

In addition, the performance of a thermal state reconstruction can also be evaluated

based on the reconstructed initial state's similarity to the ground-truth. We calculated the correlation between two thermal structures as follows:

Algorithm 1 Correlation between two thermal structures

Require: Thermal fields $T_1(x, z)$ and $T_2(x, z)$

Ensure: Correlation η

function LowPASS(T)

 Cutoff Ratio=0.2, transition width=0.4, smoothing power=4

return Filtered T

end function

$\tilde{T}_1 \leftarrow \text{LowPASS}(T_1)$

$\tilde{T}_2 \leftarrow \text{LowPASS}(T_2)$

Center the fields: $\hat{T}_1 \leftarrow \tilde{T}_1 - 0.5$

$\hat{T}_2 \leftarrow \tilde{T}_2 - 0.5$

$\eta \leftarrow \frac{\langle \hat{T}_1, \hat{T}_2 \rangle}{\|\hat{T}_1\| \cdot \|\hat{T}_2\|}$

return η

A low pass filter is applied to reduce the influence from high frequency distortions, as the critical information are those from the long wave length structure. Upon filtering the initial fields, a Cosine similarity is applied to measure the correlation between the two.

S6 INVERSE CONVECTION IN TIME WINDOW 2

The performance of inverse convection neural operator can vary significantly depending on the information preserved in the terminal thermal state. The inverse convection neural operator can stably reverse the convection in time window 2 (Fig. S7) back to more than one transit time, which is about three times longer compared with that in the nominal case using time window 3 that was described and shown in the main text. This performance of the reverse convection neural operator is evident from the correlation functions (Fig. S8a), showing that it even outperforms the joint inversion method. However, with the addition of observational noise, the inversion approach still remains the most robust method (Fig. S8b).

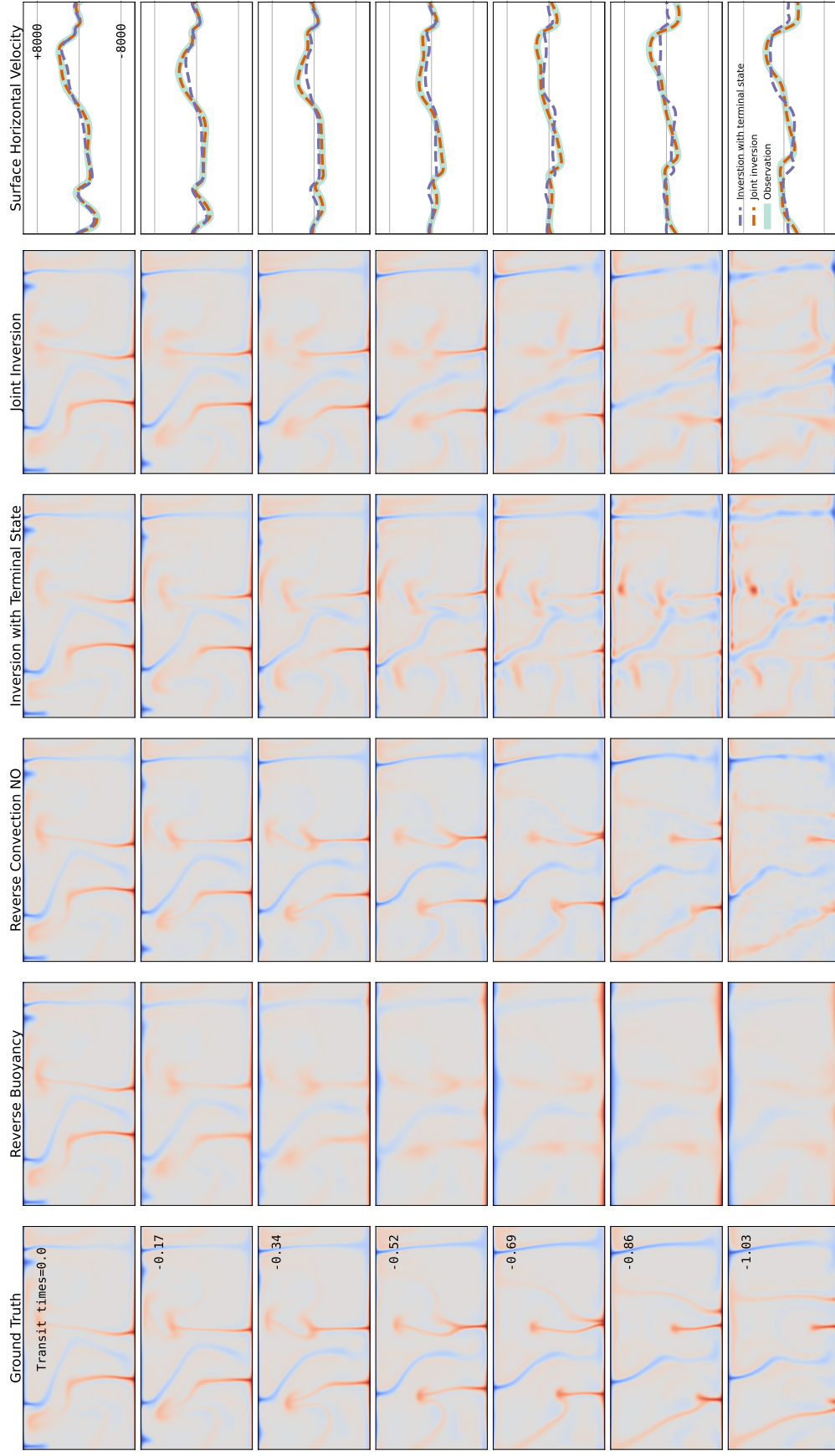


Figure S7. Thermal state reconstruction with different methods. Reversal time steps shown by row (from top to bottom backwards in time). Column 1: A ground-truth thermal convection sequence within time window 2 computed by `Underworld` forward in time from bottom to top; Column 2-5: Reconstruction with: reverse buoyancy; reverse convection operator; inversion with terminal state only; joint inversion; Column 6: Synthesized observations (clean), where the background color in the top row shows the observed terminal thermal field, and the gray curves represent the observed surface horizontal velocity profiles at each time step. The red and green curves are the predicted velocity profiles by two inversion methods.

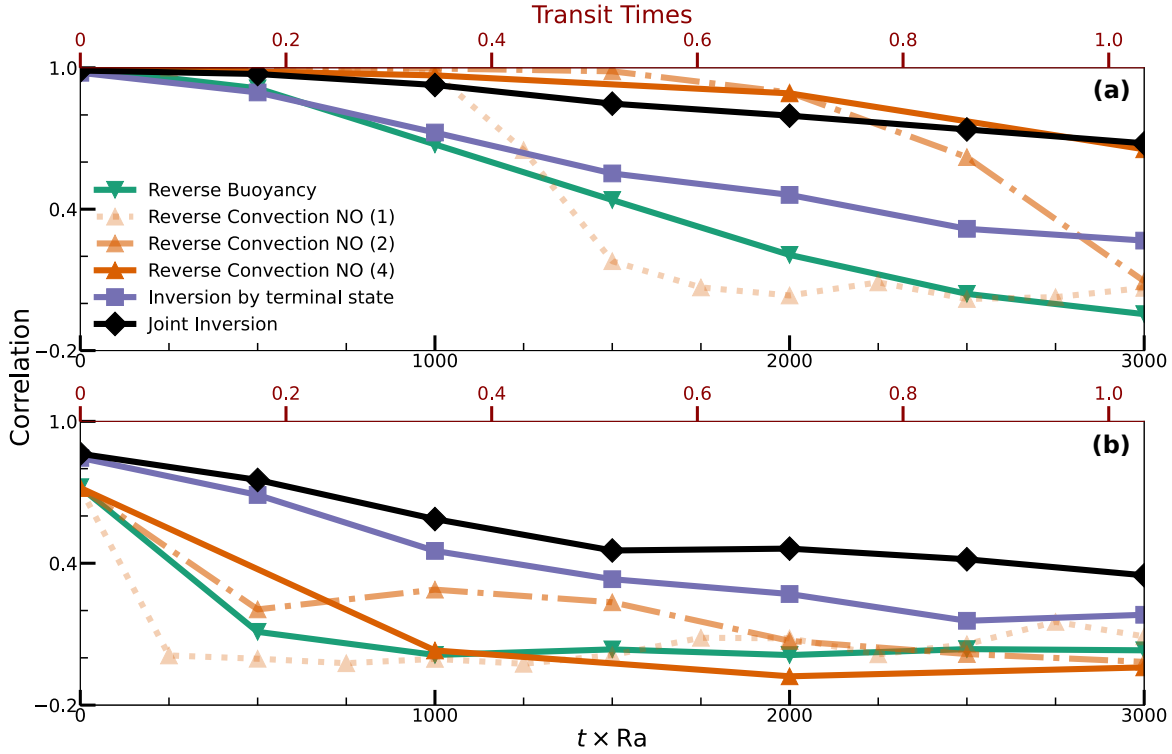


Figure S8. Correlation coefficients of reconstructed thermal fields with ground-truth fields versus backwards time within time window 2. Colored lines denote different reconstruction methods. (a) Reconstruction with synthesized observations (no noise); (b) Reconstruction with synthesized observations polluted with 5% pink noise.

S7 COMPUTATIONAL COST AND SCALING: A COMPARISON BETWEEN NEURAL OPERATOR AND NUMERICAL SOLVER BASED WORKFLOWS

How the neural operator accelerates the computation of mantle dynamics, the scaling with the size of the problem, and the relative computational cost between workflows (for forward models and time-dependent inversions) are all estimated based on traditional numerical methods and neural operators. Our problem is the integration of the thermal state, which corresponds to basic computational elements: Integrating a thermal state forward, and propagating a gradient backward in time by a specific time interval. In these estimates, the interval is set to be one transit time in our $\text{Ra} = 10^7$ case. The quantities for the cost and scaling evaluations are defined (Table S5).

First, we compared the compute times required to implement the two basic computational elements (forward and backward) using traditional numerical methods and neural operators. For numerical methods, we used the finite element method based geodynamics soft-

Symbols	Names
M	Number of nodes in each direction (assumed to be equal)
N_s	Size of problem (M^2)
N_{dof}	Degree of freedoms for the thermal convection problem
Δt	Period by which problem is integrated by
Δx_0	Grid spacing of the nominal case
Δx	Grid spacing
H	Hidden channel number in FNO
k_{max}	Cutoff frequency mode in FNO
$C_{trad,o}$	Set up cost of a traditional PDE solver
K_{trad}	Overhead of a traditional PDE solver
C_{trad}	Cost of a traditional PDE solver integrating a system forward/backward for one transit time
C_{NO}	Cost of $\mathbf{F}_{\phi 7}^{+n\Delta t}$ integrating a system forward/backward for one transit time
$C_{fwd,trad}$	Cost using a traditional PDE solver in a forward modeling problem
$C_{pretrain,NO}$	Pretraining cost using a neural operator in a forward/inversion problem
$C_{train,NO}$	Training cost using a neural operator in a forward modeling/inversion problem
$C_{fwd,NO}$	Cost of using a neural operator in a forward modeling problem
$C_{inv,trad}$	Cost of using a traditional PDE solver in a time dependent inversion problem
$C_{inv,NO}$	Cost of using a neural operator in a time dependent inversion problem
C^*	Pricing of corresponding computation demands

Table S5. Quantities used to evaluate the computational costs and the scaling of two methods.

ware **Underworld**. As described in main text, the solution of the Stokes equations and the advection-diffusion equation are interleaved as the system is integrated forward. The cost for Stokes system using the most efficient multigrid method is $O(N_{dof})$ where $N_{dof} = 3N_s$ (Moresi et al. 2003), while the advection-diffusion equation is solved with streamline upwind Petrov Galerkin method (Brooks & Hughes 1982) on the same mesh, costing $O(N_s)$. In practice, the multigrid method for the Stokes needs to be carefully tuned to reach $O(N_{dof})$. Often the time required could be slightly larger (Moresi et al. 2003). Hence, the one-step solve for the governing equations Eq. 4 to 6 approximately takes $O(N_{dof}) \sim O(N_s)$.

The maximum time step is constrained by CFL condition, which satisfies

$$\Delta t_c \sim \max \left\{ \frac{(\Delta x)^2}{\kappa}, \frac{\Delta x}{u_{max}} \right\} \sim \frac{\Delta x}{u_{max}} \propto 1/M = 1/N_s^{1/2} \quad (\text{S21})$$

As Δt_c is dependent on the current maximum velocity u_{max} in the domain, the value could

vary as convection changes, but in general, u_{max} can be regarded as constant. To integrate the system forward for a specific interval, the number of CFL time steps required is then proportional to $N_s^{1/2}$, and the total computational time required for the integration is the product of number of steps and the one-step cost

$$C_{trad}(N_s) = C_{trad,0} + K_{trad} \times N_s^{3/2}, \quad (\text{S22})$$

a trend validated by the data in Table S6.

To propagate a gradient backwards, the adjoint state equations are solved using the same numerical solvers as they share a similar forms as the forward governing equations. Consequently, the cost is the same as C_{trad} , while the overhead factor is larger than the forward integration, discussed below.

As for the neural operator based methods, the forward computation has been transformed into a forward pass through a neural network and its computational time is mainly composed of the following parts: (1) MLP layer $O(N_s H)$, (2) fast Fourier transformation $O(N_s \log N_s)$, and (3) multiplication in frequency space $O(k_{max}^2 H^2)$; thus the cost is (Table S6)

$$C_{NO}(N_s) = O(N_s H) + O(N_s \log N_s) + O(k_{max}^2 H^2) \sim O(k_{max}^2 H^2) \quad (\text{S23})$$

Usually, when k_{max}^2 is substantially smaller than N_s , the total cost is dominant by the FFT term that scales as $C_{NO} \sim O(N_s \log(N_s))$ (Li et al. 2021). However, in this study, both k_{max}^2 and H^2 are comparable to N_s in the range of consideration, and the dominant term in C_{NO} becomes $O(k_{max}^2 H^2)$, which is a constant indicative of the size of the FNO. Neural operators use auto-differentiation to compute the gradient with respect to its inputs. During this process, all the computations use the same computational graph and again are conducted in reverse, hence the backward process also has a constant time complexity as C_{NO} .

We measured the costs of integrating over one transit time with different resolutions using **Underworld** on a single CPU core and using neural operators on a GPU (Table S6). As for traditional numerical methods, Δt_c is dependent on the input thermal structures, thus we sampled inputs through out the process where a convection pattern develops from initial random fields until a steady state is achieved (Fig. 1), and averaged the cost among those cases.

Based on the measured computational costs of the two basic elements using finite element methods and neural operators, we can evaluate the total costs of the two methods under circumstances of two workflows, forward modeling and time-dependent inversion. The total

Table S6. CPU (AMD EPYC™6954) and GPU (Nvidia RTX™6000 Ada) times in seconds (s) for the numerical solver `Underworld` and forward convection neural operators by integrating the convection forward or propagate a gradient backward over one transit time.

Resolution N_s	65 ²	129 ²	257 ²	513 ²	Expected Scaling	Measured Scaling
					Exponent	Exponent
C_{trad}	25.14	260.7	1832.22	18923.46	1.5	1.58
C_{NO}	0.028	0.065	0.081	0.196	—	0.48
Speedup	897.86	4010.77	22620.00	96548.26	—	1.14

cost of numerical method-based workflow equals the cost of integrating a thermal field forward by A_F transit times

$$C_{fwd,trad}(N_s) = A_F * C_{\text{trad}}(N_s) \quad (\text{S24})$$

As for the neural operator based workflow, the cost of applying neural operators to the integration is almost negligible compared with numerical methods, due to its significant speedup (Table S6):

$$A_F * C_{\text{NO}}(N_s) \ll A_F * C_{\text{trad}}(N_s) \quad (\text{S25})$$

However, the major cost is contributed by pretraining and training. Pretraining cost can be evaluated by the total integration time when creating the training data, counted as A_T , proportional to the product of number of data pairs within training and validation dataset (shall be larger than 10^4 for each model) and the intervening time interval. The pretraining cost will be:

$$C_{\text{pretrain,NO}}(N_s) = A_T * C_{\text{trad}}(N_s) \quad (\text{S26})$$

The training datasets prepared for three forward models are sampled from a single large dataset, with a total integration time on the order of $A_T \sim 10^3$. This time interval is orders of magnitudes larger than most forward mantle dynamics models. Usually a forward modeling study has A_F ranging from less than one (e.g., subduction modeling), tens (e.g., supercontinent cycles) to at most over one hundred (e.g., Earth's secular evolution). Although multiple trials are probably required in those forward models, to train a neural operator surrogate model

might still not be worthwhile in such studies, let alone the training cost $C_{train,NO}$ shall as well be taken into consideration.

The training of neural operators is an aggregation of numerous forward and backward computation, which is a highly parallel process on GPUs. Since C_{NO} is dominant by the neural network size rather than data resolution in our case, $C_{train,NO}$ can be also assumed as a constant in our study. The training process of $\mathbf{F}_{\phi 7}^{+n\Delta t}$ takes 10^2 GPU hours on an NVidia RTX™6000 Ada GPU, such cost is on the same magnitude as the CPU cost during training data creation when $N = 257 \times 257$, assuming that one GPU hour is priced 10 times as one CPU hour. Hence:

$$C_{train,NO}^*(N_s) \sim C_{pretrain,NO}^*(257^2) \quad (S27)$$

So far, we can conclude that for forward modeling:

$$\begin{aligned} C_{fwd,NO}^*(N_s) &= C_{train,NO}^*(N_s) + C_{pretrain,NO}^*(N_s) + A_T C_{NO}^*(N_s) \\ &= C_{pretrain,NO}^*(N_s) + C_{pretrain,NO}^*(257^2) + A_T C_{NO}^*(N_s) \\ &= A_T (C_{trad}^*(N_s) + C_{trad}^*(257^2)) + A_T C_{NO}^*(N_s) \\ &> A_F C_{trad}^*(N_s) \\ &= C_{fwd,trad}^*(N_s) \end{aligned} \quad (S28)$$

We then next compare between time dependent inversion workflows using two different methods, taking the reconstruction through time window 3 as an example. Using numerical (adjoint state) methods, the total computational cost is proportional to the product of doubled forward integration time, A_F transit times, (as we need to solve both forward and adjoint equations) and the iteration times A_I :

$$C_{inv,trad}(N_s) = 2A_I A_F C_{trad}(N_s) \quad (S29)$$

Given an optimistic estimation of convergence iteration step of 10^3 to 10^4 , where the former value is estimated from a previous study using tradition numerical solvers (Li et al. 2017) (though with a shorter integration time) while the latter is derived from this study (Fig. S6), we find that:

$$A_I A_F \sim A_T \quad (S30)$$

showing that the total cost of an adjoint time-dependent inversion is about the same or larger than than the dominant term in a neural operator-based cost—the training data generation.

If neural operator is used, the training and pretraining cost has been estimated in Eq. S26 and S27. The inversion itself is remains fast and negligible (only costs several GPU hours in our case):

$$2A_I A_F C_{NO}(N_s) \ll 2A_I A_F C_{trad}(N_s) \quad (\text{S31})$$

Thus, the total cost is:

$$\begin{aligned} C_{inv,NO}^*(N_s) &= C_{train,NO}^*(N_s) + C_{pretrain,NO}^*(N_s) + 2A_I A_F C_{NO}^*(N_s) \\ &= C_{pretrain,NO}^*(N_s) + C_{pretrain,NO}^*(257^2) + 2A_I A_F C_{NO}^*(N_s) \\ &= A_T (C_{trad}^*(N_s) + C_{trad}^*(257^2)) + 2A_I A_F C_{NO}^*(N_s) \\ &\sim 2A_I A_F C_{trad}^*(N_s) \\ &= C_{inv,trad}^*(N_s) \end{aligned} \quad (\text{S32})$$

showing that cost of training a new neural operator from the beginning and then apply it to a time-dependent inversion is comparable, or even less than performing just one traditional numerical inversion. Consequently, from the perspective of time-dependent reconstructions, it costs less to build a neural operator-based workflow. Given that the savings scale up as problem size grows, one can expect that the NO workflow could provide a means to solve global mantle state reconstructions.